Distinct Patterns of Tropical Pacific SST Anomaly and Their Impacts on North American Climate

YUANYUAN GUO

Center for Monsoon and Environment Research, School of Atmospheric Sciences, Sun Yat-sen University, Guangzhou, China, and Lamont-Doherty Earth Observatory, Columbia University, Palisades, New York

MINGFANG TING

Lamont-Doherty Earth Observatory, Columbia University, Palisades, New York

ZHIPING WEN

Center for Monsoon and Environment Research, School of Atmospheric Sciences, Sun Yat-sen University, Guangzhou, China

DONG EUN LEE

Lamont-Doherty Earth Observatory, Columbia University, Palisades, New York

ABSTRACT

A neural-network-based cluster technique, the so-called self-organizing map (SOM), was performed to extract distinct sea surface temperature (SST) anomaly patterns during boreal winter. The SOM technique has advantages in nonlinear feature extraction compared to the commonly used empirical orthogonal function analysis and is widely used in meteorology. The eight distinguishable SOM patterns so identified represent three La Niña–like patterns, two near-normal patterns, and three El Niño–like patterns. These patterns show the varied amplitude and location of the SST anomalies associated with El Niño and La Niña, such as the central Pacific (CP) and eastern Pacific (EP) El Niño. The impact of each distinctive SOM pattern on winter-mean surface temperature and precipitation changes over North America was examined. Based on composite maps with observational data, each SOM pattern corresponds to a distinguishable spatial structure of temperature and precipitation anomaly over North America, which seems to result from differing wave train patterns, extending from the tropics to mid–high latitudes induced by longitudinally shifted tropical heating. The corresponding teleconnection as represented by the National Center for Atmospheric Research Community Atmospheric Model, version 4 (CAM4), was compared with the observational results. It was found that the 16-member ensemble average of the CAM4 experiments with prescribed SST can reproduce the observed atmospheric circulation responses to the different SST SOM patterns, which suggests that the circulation differences are largely SST driven rather than due to internal atmospheric variability.

1. Introduction

El Niño–Southern Oscillation (ENSO) is the most dominant mode in the coupled ocean–atmosphere system on an interannual time scale. Both the warm (El Niño) and cold (La Niña) phases of ENSO exert a large impact on the global climate (e.g., Rasmusson and Carpenter 1982; Hoerling et al. 1997; Trenberth 1997; Harrison and Larkin 1998; Larkin and Harrison 2005a,b; Chiodi and Harrison 2013; Chen et al. 2014; L'Heureux et al. 2015; Yu et al. 2015). It is well known that each individual ENSO event is unique in terms of both the sea surface temperature (SST) patterns and their climate impacts (Capotondi et al. 2015). Better understanding and characterization of the differences among the historical ENSO events and the associated climate teleconnections can be extremely useful for improved skill in regional seasonal climate prediction.

ENSO events are often defined by the tropical Pacific SST index, such as Niño-1+2, Niño-3, Niño-4, and

Corresponding author: Yuanyuan Guo, guoyyuan@mail2.sysu.edu.cn

Niño-3.4. Traditional El Niño as well as La Niña, referring to anomalous warming and cooling of the tropical eastern Pacific Ocean, are typically defined by an SST departure from normal in the Niño-3 (5°S to 5°N, 150° to 90°W) or Niño-3.4 (5°S to 5°N, 170° to 120°W) region. However, previous studies have noted that there are cases in which warm SSTs are confined farther to the west and do not reach the entire Niño-3 region (Larkin and Harrison 2005a,b). In other cases, warm SSTs extend beyond the western fringe of the Niño-4 region (5°S~5°N, 160°E~150°W) (Ashok et al. 2007). Different El Niño indices, such as El Niño Modoki (e.g., Ashok et al. 2007) and multiple Niño indices (e.g., Kug et al. 2009; Yeh et al. 2009), were proposed to capture the different flavors of El Niño. The SST-index-based methods were also proposed to define the different types of La Niña (e.g., Cai and Cowan 2009; Shinoda et al. 2011; Yuan and Yan 2013; Zhang et al. 2015), though some studies argued that La Niña events are difficult to classify into distinctive types based on SST anomaly patterns (e.g., Kug et al. 2009; Kug and Ham 2011; Ren and Jin 2011).

Another commonly used method for identifying El Niño events is the empirical orthogonal function (EOF)-based method (e.g., Ashok et al. 2007; Kao and Yu 2009). The index-based method suffers from its subjectivity in picking the indices, while the EOF-based method assumes linearity and orthogonality among different modes (e.g., Johnson 2013; L'Heureux et al. 2013). To overcome these difficulties, the self-organizing maps (SOM) method was introduced to identify the different types of ENSO events (e.g., Singh 2012; Johnson 2013; Li et al. 2015). The biggest advantage of the SOM analysis is its ability to extract nonlinear and asymmetric features of any spatial–temporal-varying field (Lin and Chen 2006; Liu et al. 2006; Iskandar 2009; Li et al. 2015). The asymmetry between the two ENSO phases and the different flavors of El Niño and La Niña SST patterns may be an indication of nonlinearities in the coupled ocean–atmosphere system (Choi et al. 2011; Takahashi et al. 2011; Graham et al. 2014). Some previous efforts have been made to distinguish different flavors of ENSO events using the SOM technique. Most devoted the effort to the classification of different ENSO patterns (e.g., Singh 2012; Johnson 2013; Li et al. 2015), the cycle of different contiguous ENSO events (Li et al. 2015), trend analysis (e.g., Singh 2012; Johnson 2013), transition processes between warm and cold ENSO phases (Leloup et al. 2007), and hydrological response to distinguishable ENSO events (Xu et al. 2015). Few studies focus on the impact of distinct ENSO patterns on the extratropical teleconnection and climate variability using the SOM method. Because of the crucial importance of ENSO teleconnection and its possible sensitivity to different SST

anomaly patterns, the continuous classification of ENSO events using SOM and the associated teleconnection patterns could further improve ENSO-based climate forecast. Consequently, the focus in the present study is on the continuously varying ENSO flavors as identified by the SOM method and their impact on extratropical ENSO teleconnection in winter.

Previous studies have examined the impact of different ENSO flavors on the North American climate (e.g., Mo 2010; Yu et al. 2012; Garfinkel et al. 2013; Yu and Zou 2013; Yu et al. 2015; L'Heureux et al. 2015; Infanti and Kirtman 2016) using either the SST-indexes or EOF-based methods. While the canonical El Niño event is associated with warm temperature anomalies over western Canada and the northern United States and cool anomalies over the southern and eastern tiers of the United States, with a general reversal in the pattern of surface temperature anomalies during La Niña (Ropelewski and Halpert 1986; Hoerling et al. 1997; Larkin and Harrison 2005a; Lau et al. 2008; Zhang et al. 2011; Chiodi and Harrison 2013), some studies showed that central Pacific (CP) and eastern Pacific (EP) El Niño are associated with differing teleconnection patterns and the North American climate anomalies (e.g., Yu et al. 2012; Yu and Zou 2013; Zou et al. 2014). The identifications of different ENSO types, however, largely depend on the methods used. Hence, there is a need to examine the robustness of the climate patterns associated with continuous ENSO flavors by investigating the influence of differing SOM patterns on climate teleconnections over North America and the robustness of the sensitivity. Furthermore, we examine the robustness of the teleconnection sensitivities to differing SST patterns using the state-of-the-art atmospheric general circulation models (AGCMs) with prescribed historical SST evolution. The comparison between model and observations provides further support that the sensitivity in atmospheric teleconnections to different SOM SST patterns shown in observations may be SST driven. In addition, some studies have noted that the internal variability of the atmospheric climate system is greatly important for leading to the observed inter–El Niño variation (Kumar and Hoerling 1997). They argued that the distinctive atmospheric response from one ENSO event to another at the mid–high-latitude are primarily driven by the internal atmospheric variability, though inter-event variation in SST anomaly the amplitude and spatial structure also matters. Thus, the role of internal atmospheric variability in explaining the different ENSO teleconnections and North American climate impacts should be further investigated.

The rest of the paper is organized as follows. Datasets and methods are described in section 2. In section 3, the

classification of the SST anomaly patterns in the tropical Pacific using the SOM technique is presented. Section 4 describes the impact of the SOM patterns on winter-mean surface temperature and precipitation changes over North America. In addition, the results obtained from the observation and an atmospheric general circulation model are compared, followed by a summary and discussion in section 5.

2. Datasets and methods

a. Observations and model data

The datasets used to generate the winter [December–February (DJF)] averages in the present study consist of the 1) monthly mean Hadley Centre Sea Surface Temperature (HadISST; Rayner et al. 2003) for the period from 1856 to 2013; 2) CRU, version 3.23, of monthly temperature and precipitation over global land areas from the Climatic Research Unit at the University of East Anglia (Harris et al. 2014) with a horizontal resolution of 0.5° from 1901 to 2010; 3) global land precipitation data from the Global Precipitation Climatology Centre (GPCC; Rudolf et al. 2010) for the period from 1901 to 2010 at 1.0° grid resolution; 4) Twentieth Century Reanalysis, version 2 (20CRv2) data provided by the NOAA/OAR/ESRL PSD, Boulder, Colorado (which is available at http://www.esrl.noaa.gov/psd/) for 1901–2010 (Compo et al. 2011); 5) ECMWF's atmospheric reanalysis of the twentieth century (ERA20C) (which can be downloaded at http://apps.ecmwf.int/datasets/data/era20c-moda/levtype=sfc/type=an/) from 1901 to 2010 (Poli et al. 2013); 6) NOAA interpolated outgoing longwave radiation (OLR) from 1975 to 2010 (Liebmann and Smith 1996), which was only used as a comparison to precipitation data derived from ERA20C.

The AGCM used in this study is the National Center for Atmospheric Research (NCAR) Community Atmospheric Model, versions 4 and 5 (CAM4 and CAM5). We used output from the 16-member Global Ocean Global Atmosphere (GOGA) experiments where the observed Hadley center SST and sea ice (Rayner et al. 2003) for the period 1856–2008 (1856–2013 for CAM5) is prescribed over the global oceans. The main differences between CAM4 and CAM5 are the physics and the cloud parameterizations, including shallow convection, microphysics, macrophysics, radiation, and aerosols (Neale et al. 2010, 2012). We use both the 16-member ensemble mean (represents the SST-forced responses) and the ensemble member spread (represents the internal atmospheric variability) in our analysis.

To incorporate the increasing ocean temperature in the last 100 years, the SST anomalies are obtained by removing the climatology of the moving 30-yr periods,

which are updated every five years (L'Heureux et al. 2013; Li et al. 2015). The SST anomalies obtained this way are similar to applying linear detrending, but it effectively removes the SST warming trend as well as the interdecadal change in the oceanic variability and focuses on the interannual ENSO variation.

b. SOM technique

The SOM technique, which consists of neurons organized on a regular low-dimensional grid, is a type of unsupervised artificial neural-network-based cluster analysis (Kohonen et al. 1995; Kohonen 1998, 2001; Johnson et al. 2008). The SOM analysis has been increasingly applied to atmospheric and ocean sciences in the past 15 years (e.g., Hewitson and Crane 2002; Richardson et al. 2003; Liu et al. 2006; Leloup et al. 2007; Johnson 2013). During the SOM training process, the input SST data are projected to a set of neural networks nodes (the so-called units). For every unit, there is a weight vector, which is a weighted average of the input SST fields for different nodes or clusters. The classification of SST anomaly patterns for every year is determined by the relative magnitude of the Euclidian distance between the weight vector of each unit and the input SST data. The unit whose weight vector is closest to the input SST data (viz., the smallest Euclidian distance) is selected as the "winner" (best matching unit) after repeated iterations. More details on SOM methodology and the appropriate parameter choices are given in Vesanto et al. (2000) and Liu et al. (2006).

The SOM analysis has several advantages. For example, it is able to extract nonlinear and asymmetric features (Liu et al. 2006; Iskandar 2009). It has been shown that SOM is more robust than principal component analysis in identifying predefined patterns when applied to the synthetic datasets (Reusch et al. 2005; Li et al. 2015). In the present work, the SOM analysis is applied to observed SST in the tropical Pacific domain, which covers the area 25°S to 25°N, 120°E to 80°W. The time period for the analysis is from 1901 to 2010 for this study, although analyses were also applied to the entire length of the data, 1856–2013, for sensitivity testing. All SOM calculations are performed with the Matlab SOM toolbox (Vesanto et al. 2000; available at http://www.cis.hut.fi/somtoolbox/.).

c. False discovery rate

For most cluster analyses including the SOM method, the cluster number K must be specified prior to the analysis. Thus, some efforts have been made to determine the optimal number of clusters (e.g., Michelangeli et al. 1995; Christiansen 2007; Hastie et al. 2009; Johnson 2013; Riddle et al. 2013). A field significance approach, named

"false discovery rate" (FDR), was used to determine whether two cluster patterns are statistically distinguishable. More detailed descriptions of the method can be found in several previous studies (e.g., Benjamini and Hochberg 1995; Wilks 2006; Johnson 2013). In this study, we followed the method used by Johnson (2013). First, we computed the composited SST anomalies for K SOM patterns. Then for these K SOM cluster patterns, there are $C_K^2 = K(K-1)/2$ possible pairs of patterns to compare based on the FDR. To determine the optimal K, the SOM was applied to various values of K that increase from 2 to 20 at an increment of 1. We then use the FDR tests for each value of K and count the number of SOM pairs that are statistically indistinguishable. The largest number of K clusters with zero indistinguishable SOM pairs is the optimal number of cluster patterns. The SOM training process requires a map size (number of units K) specification, which can be either a one-dimensional or two-dimensional array. We use a map size of $1 \times K$ ($K = 2, 3, \ldots, 20$) to perform the SOM technique, named one-dimensional SOM.

3. Different flavors of ENSO events

The method described in section 2 was first applied to determine the optimal K clusters. The number of statistically indistinguishable clusters as a function of K is shown in Fig. 1. For K from 2 to 8, all pairs of SST cluster patterns remain statistically distinguishable, as the number of indistinguishable pairs (vertical axis) equals zero. The number of indistinguishable pairs rises above 0 for K equal to or greater than 9, which means the optimal K is 8 SOM patterns.

Figure 2 shows the eight distinguishable SOM patterns (the weight vectors). The occurrence frequency of each pattern is shown in the upper right in Fig. 2. The first three clusters (Figs. 2a–c) illustrate three La Niña–like patterns with differing SST anomaly amplitudes and very slightly shifted maximum SST anomaly location. Previous studies questioned whether there exists more than one distinguishable type of La Niña (e.g., Kug et al. 2009; Kug and Ham 2011; Yuan and Yan 2013; Zhang et al. 2015). Figure 2 indicates that the SOM is able to distinguish different flavors of La Niña, not as much by their longitudinal locations of the SST anomalies but by the SST anomaly strength. The last three clusters (Figs. 2f–h) feature continuous changes from a weak CP El Niño pattern to a canonical EP El Niño pattern. In addition to differences in the longitudes of maximum SST anomalies, there are also amplitude differences. The transition pattern (P7) from CP (P6) to EP (P8) has mixed characteristics of both (CP2), which is characterized by a maximum warming in the central and
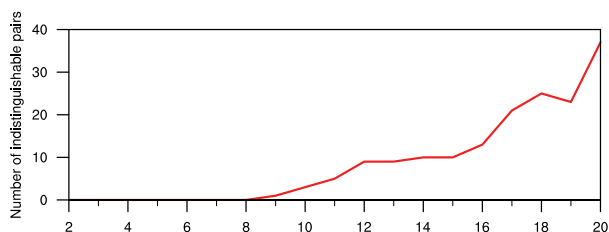

FIG. 1. The number of SOM SST cluster pattern pairs that are indistinguishable at the 95% confidence level. The horizontal axis indicates the number of SOM patterns K from 2 to 20.

eastern Pacific (e.g., Kao and Yu 2009; Johnson 2013). Patterns 4 and 5 exhibit very weak SST anomalies in the equatorial Pacific (Figs. 2d,e) and hence represent near normal conditions. Similar SOM patterns were identified in Johnson (2013), where they identified nine statistically distinguishable patterns using extended winter (September–February) SST data from 1950 to 2011. The largest difference between Johnson (2013) and results here is that the canonical El Niño SOM contains only three events in Johnson (2013), while our analysis identified 17 cases (15%) for the period 1901 to 2010. Given the different data length and season used in Johnson (2013) and this study, it is perhaps not surprising that there may be differences in the SOM identification. The SOM analysis was also applied to the longer period of 1856 to 2013, the entire period for which the SST data are available. The patterns identified (not shown) are almost identical to that in Fig. 2, further illustrating that when sufficiently long data are used, the SOM patterns identified are insensitive to the data length.

Figure 3 shows the Niño-3.4 index for each year color-coded by the eight SOM patterns. The EP El Niño events (P8) exhibit relatively strong warming anomaly, with Niño-3.4 index values generally exceeding 0.8°C. The Niño-3.4 index values for CP2 El Niño (P7) are mostly greater than 0.5°C but somewhat weaker than that of the EP El Niño. For the CP El Niño events as identified as P6, only 2 out of the 12 events have Niño-3.4 values above 0.5°C. Both Yu et al. (2012) and Larkin and Harrison (2005a,b) provided a list of major El Niño events since 1950 using various definitions of the different flavors of El Niño. Some events that have been widely agreed upon as the EP El Niño include the winters of 1951/52, 1969/70, 1972/73, 1976/77, 1982/83, and 1997/98 and those agreed upon as the CP El Niño include 1963/64, 1968/69, 1977/78, and 1994/95. Our results show some disagreements of ENSO classification with the studies mentioned above (Larkin and Harrison 2005a,b; Yu et al. 2012), owing to the different methods used and the more continuous characterization of CP
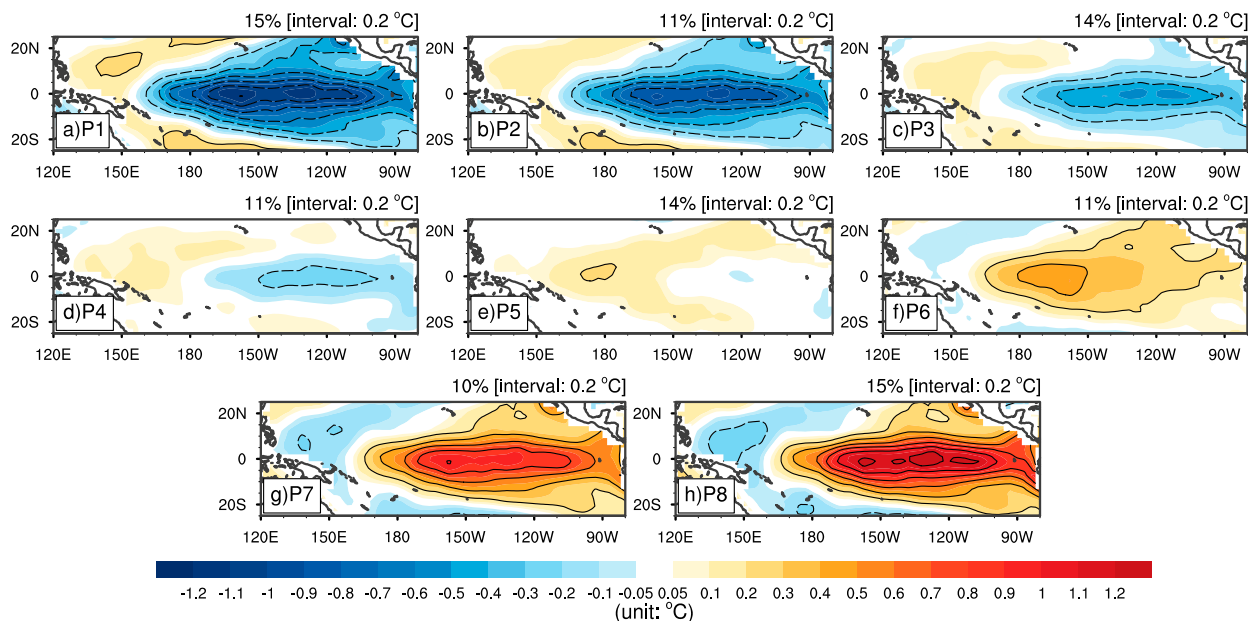
FIG. 2. The spatial distribution of eight SOM patterns (°C). The percentage to the top right of each map refers to the frequency of occurrence of the pattern for the 1901–2010 period.

and EP events with the added CP2 type. Upon further examination of those winters that show discrepancies in ENSO classification, it was found that the SOM analysis tends to provide a more realistic match of the SST patterns. For example, the DJF SST anomaly patterns in 1969/70 and 1976/77 winters (figures not shown), identified as EP El Niño in previous studies, exhibit the maximum SST warming anomalies located in the central and eastern Pacific, which is similar to the CP2 SST pattern 7. The corresponding Niño-3.4 values for the three La Niña patterns in Fig. 3 exhibit a similar tendency as its counterpart for El Niño, in that P1 (16 events) is

dominated by relatively strong negative Niño-3.4 SST anomalies, followed by P2 (12 events). Only 4 out of 15 P3 events exceed the 0.5°C Niño-3.4 threshold. Furthermore, none of the P4/5 events exceeded the 0.5°C Niño-3.4 threshold.

Figure 4 shows the composites of the DJF-mean SST anomalies corresponding to each of the SOM patterns for years when Niño-3.4 SST anomalies are above 0.5°C for any consecutive three-month averages (NOAA definition). The near-normal SOM patterns (P4 and P5) had very few or no events with any three-month-mean Niño-3.4 SST anomaly equaling or exceeding 0.5°C and
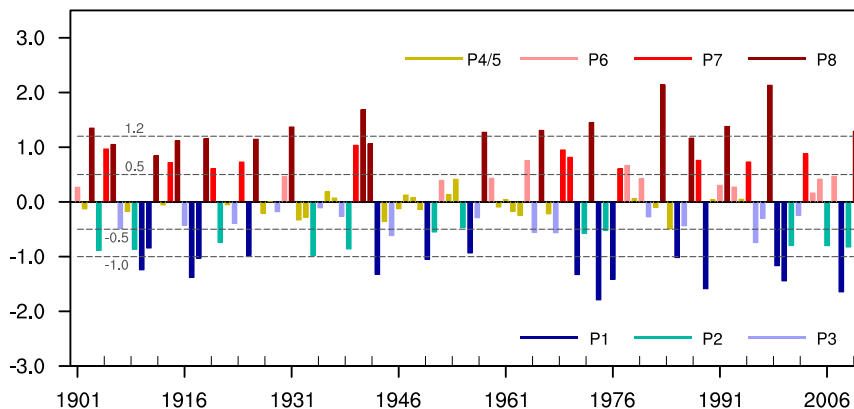

FIG. 3. The time series of DJF-mean Niño-3.4 index (°C) from 1901 to 2010 color-coded according to each year's corresponding SOM pattern identification. Warm colors, cold colors, and yellow bars indicate El Niño–like, La Niña–like, and near-normal patterns, respectively. The dashed gray lines indicate the threshold Niño-3.4 values for El Niño (+0.5°C), La Niña (−0.5°C), strong El Niño (+1.2°C), and strong La Niña (−1.0°C) used in this study.
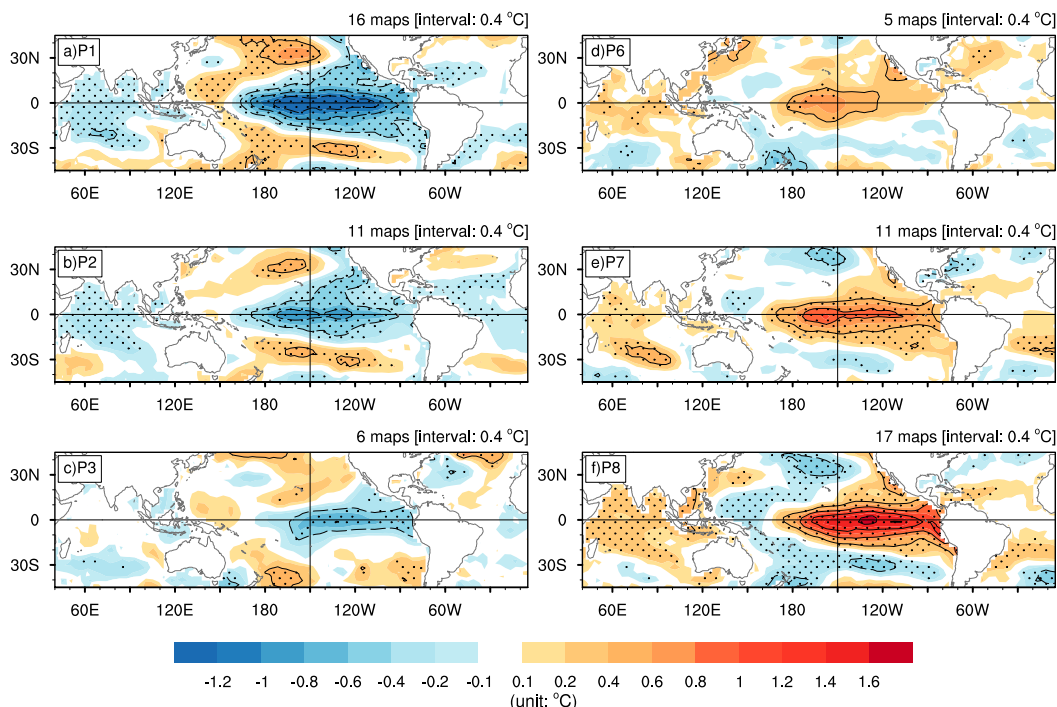
FIG. 4. Composite maps of the DJF-mean SST anomalies (°C) based on (left) La Niña–like (P1–P3) and (right) El Niño–like (P6–P8) patterns. The composite analysis involves only the years in which the winter-mean Niño-3.4 index was greater (less) than 0.5°C (−0.5°C). The stippling indicates significance at or above the 90% confidence level using the two-tailed nonparametric Monte Carlo bootstrap statistical significance test. The number at the top right of each map refers to the pattern occurrence for the period of the analysis (1901–2010). The related tropical SST anomaly patterns of near-normal cases (P4 and P5) are not shown.

are thus not shown. The dots in Fig. 4 indicate where SST anomalies pass the 90% confidence level using the two-tailed nonparametric Monte Carlo bootstrap statistical significance test. As expected, the composite SST anomaly spatial structures are similar to the original SOM patterns in Fig. 2. For patterns 1–3, the maximum cold SST anomaly in tropical Pacific ranges from strong to weak with little change in its longitudinal locations except for P3, which has a weak SST anomaly centered in the eastern tropical Pacific. All three La Niña patterns show a horseshoe-shaped pattern with cooling anomalies in the equatorial central-eastern Pacific and warming anomalies in its fringe and the North Pacific. Additionally, the two strong La Niña cases (P1 and P2) are accompanied by a basin-wide cooling in the Indian Ocean. For the three El Niño patterns, there are both SST anomaly amplitude and location differences from a weak warming of 0.6°C at 170°W (Fig. 4d), to the central-eastern tropical Pacific warming of 0.8°C centered at 150°W (Fig. 4e), to the canonical eastern tropical Pacific warming pattern with maximum SST anomaly of 1.6°C located at 120°W (Fig. 4f). A majority of the El Niño events during this period falls to the canonical EP patterns with 17 total

events, compared to 11 events for CP2 and only 5 for CP. As for La Niña, all three El Niño SST anomaly patterns show compensating cooling surrounding the warming center and weak warming in Indian Ocean and the tropical Atlantic.

It is well known that tropical convection anomalies provide the link between tropical SST anomalies and the extratropical atmospheric circulation change through poleward-propagating Rossby waves from low to mid–high latitudes (e.g., Horel and Wallace 1981; Hoskins and Karoly 1981; Simmons 1982). The tropical precipitation anomalies associated with the six SOM patterns are shown in Fig. 5 using the ERA20C reanalysis. To evaluate the ERA20C tropical precipitation, the composite OLR anomalies based on the NOAA OLR dataset for 1975–2010 for eight SOM patterns (not shown) are compared with that based on the ERA20C precipitation for the same period. The spatial patterns based on the two tropical convection measures are very similar to each other with spatial pattern correlations of 0.7 to 0.9. Also shown in Fig. 5 are contours of the vertically integrated diabatic heating from ERA20C. The almost perfect match between precipitation and vertically integrated diabatic heating shows that precipitation is a
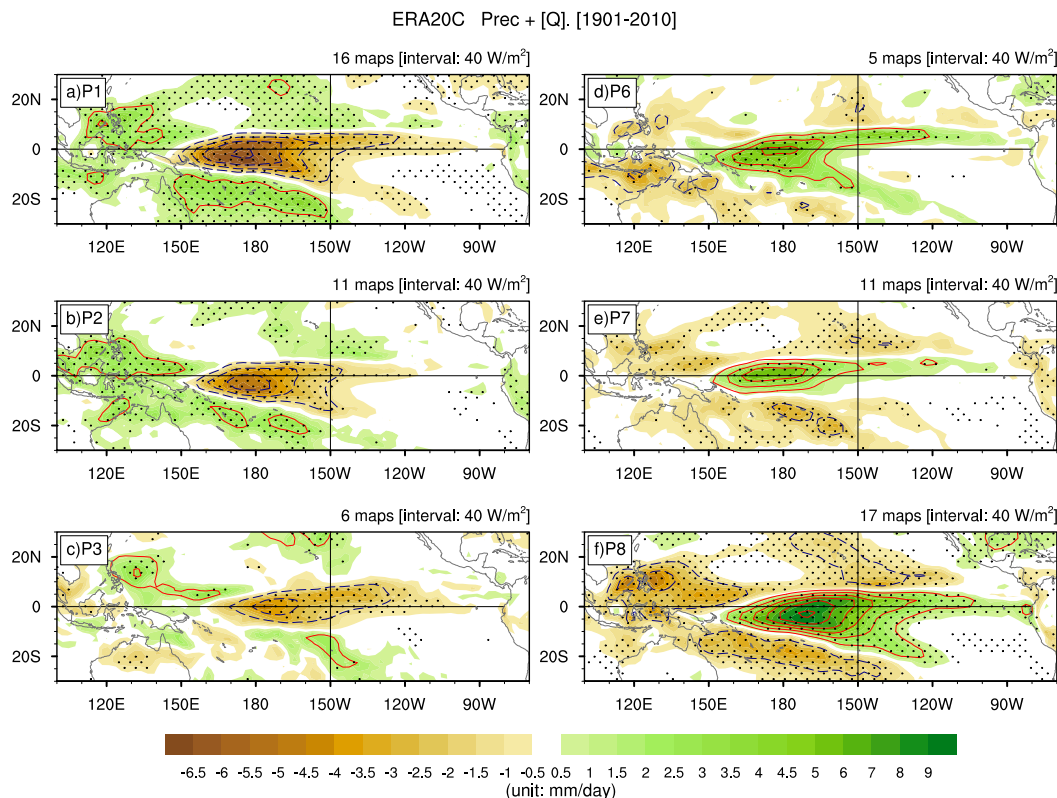
ERA20C   Prec + [Q]. [1901-2010]

FIG. 5. Composite maps of the DJF-mean tropical precipitation anomalies (shading; mm day^{-1}) and diabatic heating anomalies integrated from 1000 to 200 hPa (contour; W m^{-2}) based on (left) La Niña (P1–P3) and (right) El Niño (P6–P8) patterns, from ERA20C reanalysis data for the period of 1901–2010. The stippling indicates significance at the 90% confidence level using the two-tailed nonparametric Monte Carlo bootstrap statistical significance test, and the number at the top right of each map indicates the number of pattern occurrences during the period. The contour interval for diabatic heating is 40 W m^{-2}.

good approximation of tropical diabatic heating associated with SST anomalies.

The patterns of anomalous convection follow that of the SST anomaly patterns but shifted toward the west with respect to the corresponding SST anomaly locations, owing to the east–west asymmetry in the climatological SST distributions with warm pool to the west and cold tongue to the east. There is a distinct longitudinal shift of the anomalous convection centers across both the El Niño and La Niña patterns. A systematic eastward shift of the suppressed convection center in La Niña patterns P1 to P3 can be clearly seen in Figs. 5a–c. Note that the anomalously lower heating over the central Pacific shifts farther westward as the La Niña event gets stronger as expected. For El Niño patterns 6 and 7, the shift in positive convection is not as obvious, but there is a clear eastward shift from pattern 7 to pattern 8. The convection shifts farther eastward with a stronger El Niño event, whereas a westward shift of tropical convection is observed with a stronger La Niña, thus

creating an asymmetry between strong El Niño and strong La Niña events.

To determine whether each of the identified El Niño and La Niña patterns are indeed distinguishable from each other in terms of SST and the corresponding tropical convection anomalies, Fig. 6 shows four pairs of difference maps for the six SOM modes for SST and column-integrated diabatic heating. The statistical significance of the differences was estimated using the nonparametric Monte Carlo bootstrapping method. All four difference maps show spatially coherent and statistically significant differences for both the SST and diabatic heating, with relatively small-amplitude differences between P1 and P2 and between P6 and P7. Because of the small number of events for P3 and P6 and the relatively small amplitude in anomalous SST (Figs. 4c,d), however, the climatic impact of these two patterns were generally not statistically significant. In the following, we focus on the four patterns (two La Niña P1 and P2 and two El Niño P7 and P8)
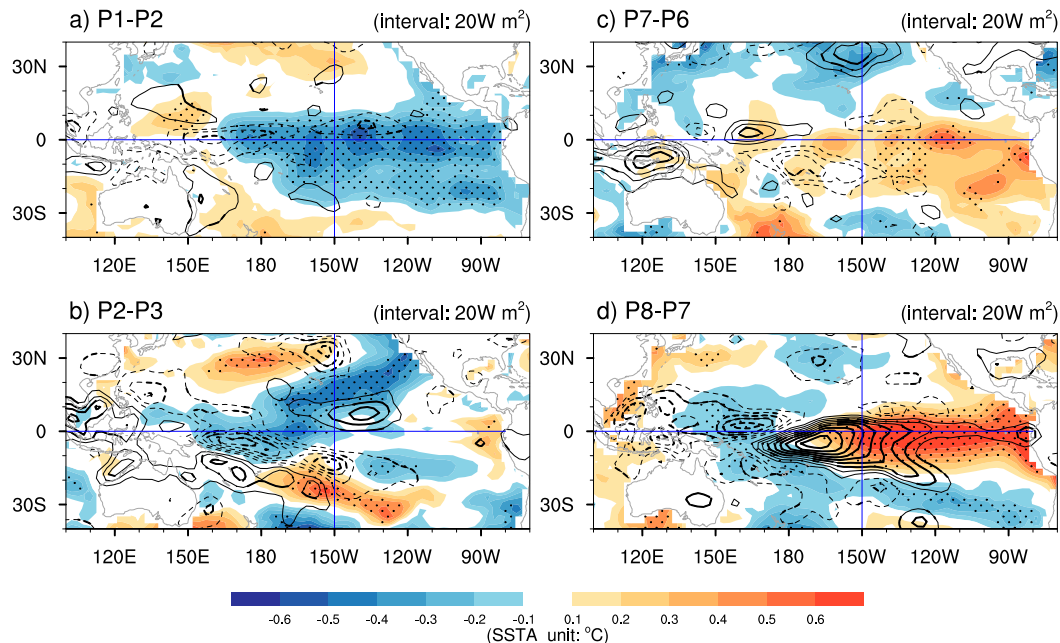
FIG. 6. The difference of SST anomaly (shaded) and vertical integrated diabatic heating (contour) among (left) La Niña (P1 − P2 and P2 − P3) and (right) El Niño patterns (P7 − P6 and P8 − P7). The stippling and thick contour indicate differences at or above the 90% confidence level using the two-tailed nonparametric Monte Carlo bootstrap statistical significance test.

for the atmospheric teleconnections and climatic impacts.

4. Impact of different ENSO patterns on North American climate

a. Observational results

To detect whether different flavors of ENSO have a distinct influence on the winter-mean climate over North America, the composite maps of surface temperature and precipitation anomalies associated with four ENSO clusters using observational data are examined. Three different observation-based surface temperature products (CRU, ERA20C, and 20CRv2) are used. The composite maps based on CRU surface temperature data are displayed in Fig. 7 and that based on the ERA20C in Fig. 8. The 20CRv2 composite maps are very similar to that of ERA20C and are thus not shown here. For La Niña pattern 1, the anomalous SST pattern produces a significant cold northwest–warm southeast anomaly pattern (Figs. 7a and 8a). For La Niña pattern 2, however, the surface temperature anomalies are less significant overall, although there is an indication of a cold north–warm south pattern with zero line across the 50°N latitude (Figs. 7b and 8b). The distinction between the temperature responses to the two La Niña patterns is mainly in the northwest North America where opposite-sign temperature anomalies

are observed but not statistically significant (Figs. 7c and 8c). For the warm ENSO phase, however, Figs. 7d,e show distinct patterns of surface temperature anomalies over North America, with an east–west pattern for CP2 (P7) and a north–south pattern for EP (P8). The CP2 composite shows a significant cold east–warm west pattern for the United States and general warming for Canada (Figs. 7d and 8d). For the EP pattern (P8), there is a significant warm north–cold south anomaly pattern (Figs. 7e and 8e), with a zero line at approximately 40°N. The north–south pattern for EP El Niño is similar to the seesaw pattern identified as the impact of El Niño on the North American temperature change in winter (e.g., Ropelewski and Halpert 1986; Hoerling et al. 1997; Larkin and Harrison 2005a; Zhang et al. 2011). The differences between P8 and P7 (P8 − P7; Figs. 7f and 8f) are spatially coherent and statistically significant across the northern plains and the northeast with stronger warming in these regions while there is less warming for the southwest for P8 compared to P7. The sensitivity of surface temperature response over North America to different types of El Niño has been discussed in previous studies. For example, Yu et al. (2012) found that winter temperature anomalies exhibit a warm northeast–cold southwest (warm northwest–cold southeast) pattern for EP (CP) El Niño events, using the regression-EOF method (Kao and Yu 2009; Yu and Kim 2010). Our results are slightly different from Yu et al. (2012) regarding
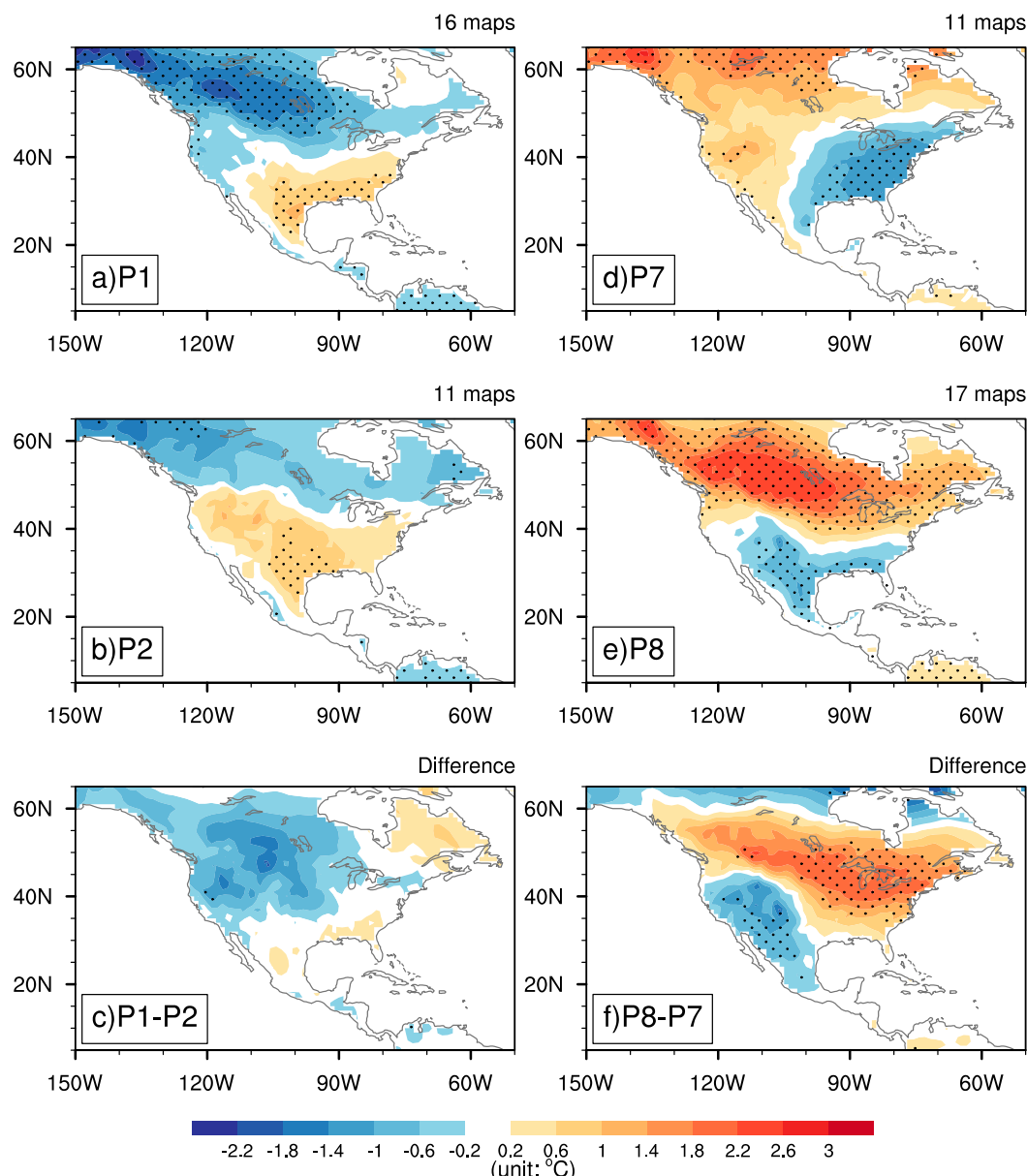
CRU   Surface temp. [1901-2010]

FIG. 7. Composite maps of the DJF-mean surface temperature anomalies over North America (°C) for (left) the two La Niña patterns (P1 and P2) and their differences and (right) the two El Niño (P7 and P8) patterns and their differences, based on CRU observational data for the period 1901–2010. Stippling indicates values at or above the 90% confidence level using the two-tailed nonparametric Monte Carlo bootstrap statistical significance test.

the EP responses, possibly owing to the different methods used to identify EP and CP events, but confirm that large sensitivities exist to the different types of El Niño. Other studies have grouped the El Niño events into OLR and non-OLR cases (e.g., Chiodi and Harrison 2013, 2015; Johnson and Kosaka 2016) and found sensitivity of North American surface temperature patterns to convective versus nonconvective EP

warming events. The composite pattern based on the nonconvective (convective) EP events in Johnson and Kosaka (2016), for example, is similar to that for P7 (P8) in our work. Hence, their nonconvective EP warming events may share similar characteristics with our CP2 pattern. The mechanisms for the surface climate sensitivity to the different El Niño patterns will be discussed later.
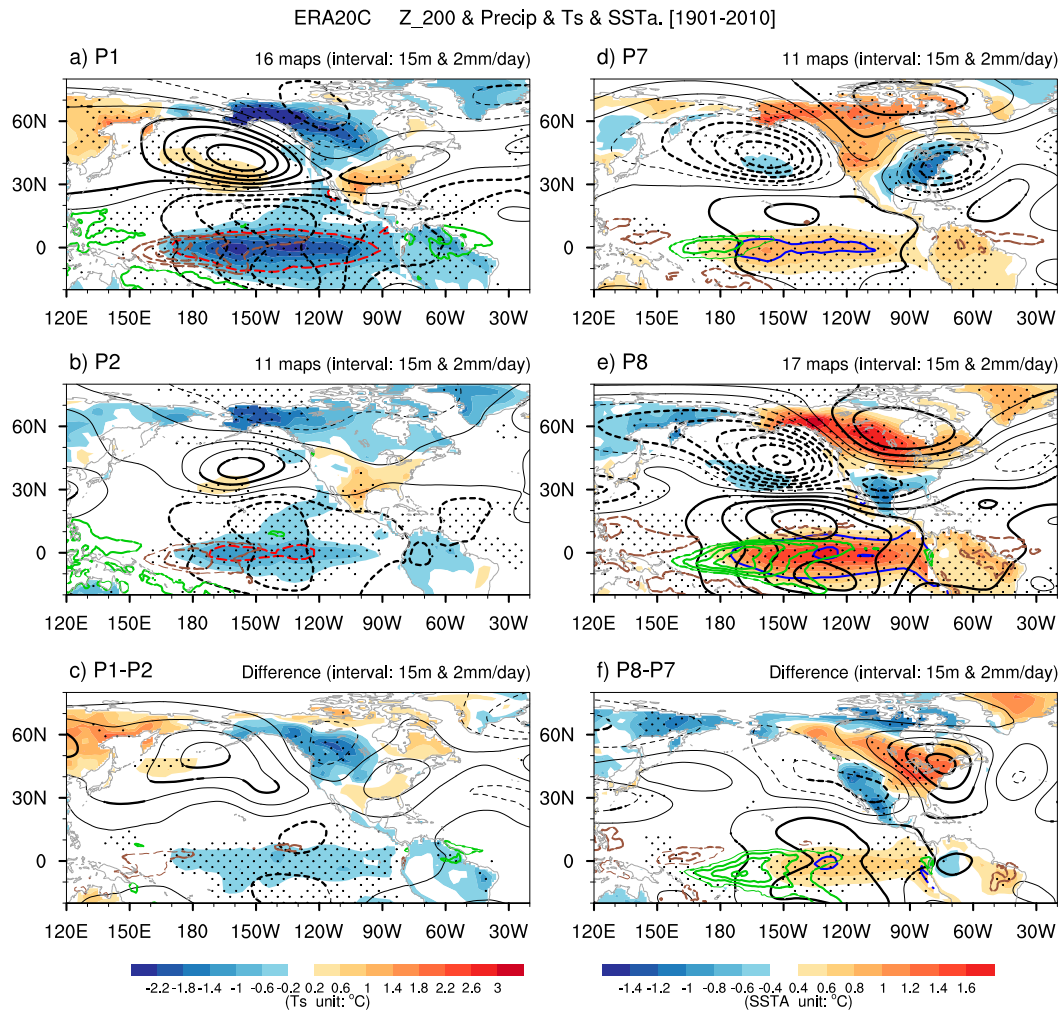
ERA20C   Z_200 & Precip & Ts & SSTa. [1901–2010]

FIG. 8. Composite maps of the DJF-mean geopotential height anomalies at 200 hPa (black contours; interval: 15 m) and precipitation anomalies (brown and green contours; interval: 2 mm day^{-1}) for (a),(b) the two La Niña patterns and (c) their differences and (d),(e) the two El Niño patterns and (f) their differences. The shading represents surface temperature anomaly over land (°C) and SST anomaly over the oceans (°C). The blue and red contours show the SST anomaly of ±0.8° and ±1.6°C. The thick contours and stippling indicate values at or above the 90% confidence level using the two-tailed nonparametric Monte Carlo bootstrap statistical significance test. All the variables, except SST (from HadISST), were derived from ERA20C for the period of 1901–2010.

The influence of ENSO events on precipitation changes is similarly shown in Figs. 9 and 10 for GPCC and ERA20C, respectively. The CRU and 20CRv2 precipitation data were also analyzed, and the results are not substantially different from that shown in Figs. 9 and 10. In general, the precipitation anomaly amplitude is larger in ERA20C as compared to GPCC, possibly owing to systematic bias in the reanalysis precipitation assimilation. Other than the amplitude difference, the spatial structures of the precipitation anomalies associated with each SST pattern are rather similar between ERA20C and GPCC. For EP El Niño (P8) and strong La Niña patterns (P1), a north–south dipole was found in Figs. 9a,e and 10a,e. The patterns are largely significant

and rather linear with respect to the ENSO phases, except for a strong wet anomaly extending from the southwest toward the central Plains in P8 (Fig. 9e) as compared to the corresponding dry extension in P1 (Fig. 9a). While the north–south dipole pattern remains for the La Niña pattern 2 (Fig. 9b) with less statistical significance in the north and more significance to the southwest as compared to P1, the CP2 El Niño pattern 7 shows a very different precipitation anomaly pattern over North America, with very little wet anomalies in the south and predominantly dryness across North America (Fig. 9d). For example, along the U.S. East Coast and the central plains, the CP2 pattern is associated with generally drying conditions (Fig. 9d), while the EP pattern is
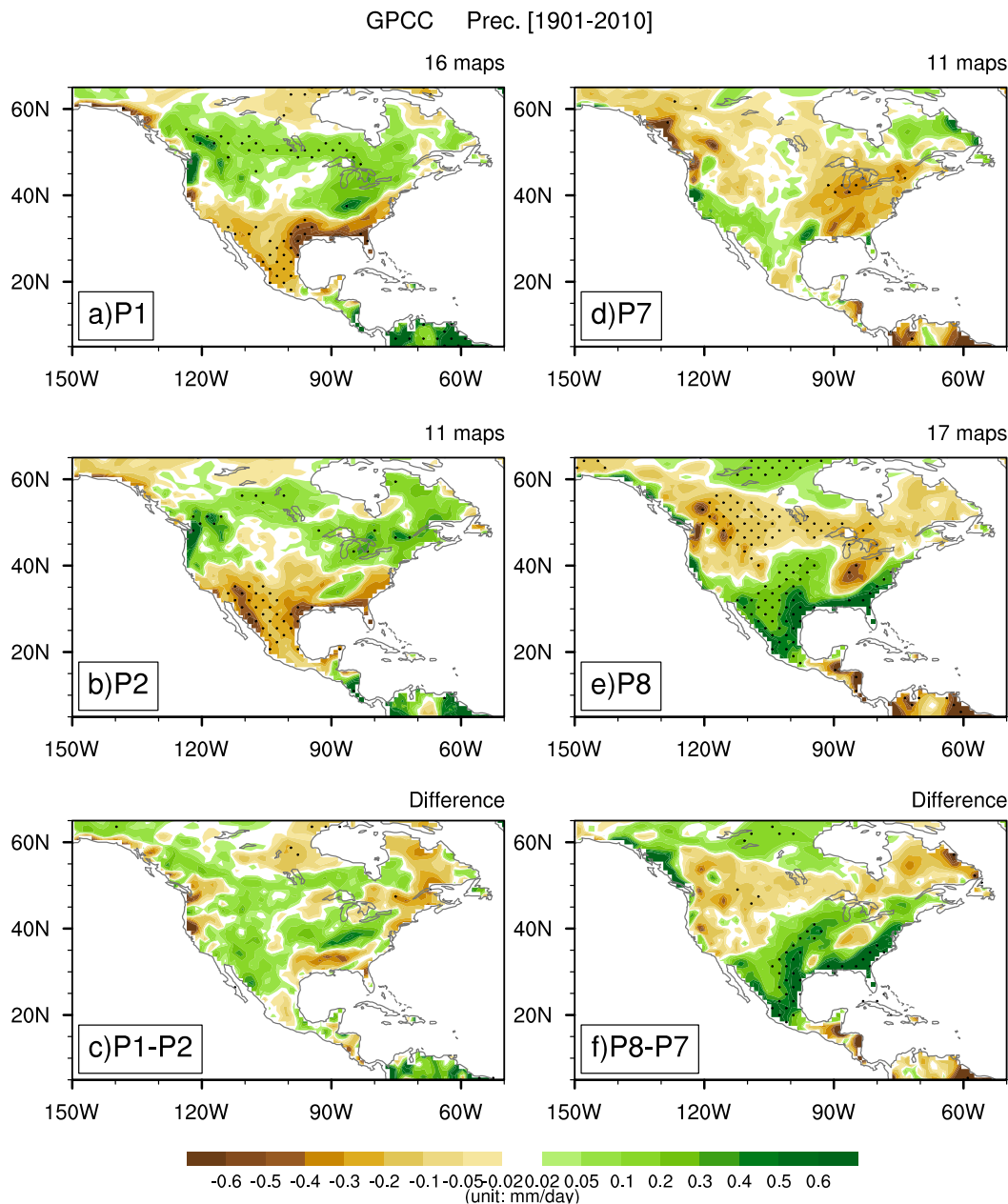
FIG. 9. As in Fig. 7, but for precipitation composites based on GPCC dataset for the period of 1901–2010.

associated with significant wetness (Fig. 9e). This contrast is clear both in the GPCC (Figs. 9f) and ERA20C (Figs. 10f). Such detailed information could be important for accurate precipitation predictions associated with an El Niño for these regions. The significance of the precipitation anomaly for CP2 (Fig. 9d) is not coherent, however. A similar composite based on EP/CP events since 1950 (Fig. 2 of Yu and Zou 2013) suggests that the dry anomalies over northern North America are more significant than in Fig. 9d, showing the dependence of the results on the identification methods

used. The differences between the two La Niña patterns (Figs. 9c and 10c) are less significant, consistent with the less distinguishable tropical convections (Fig. 6a) between P1 and P2.

To understand the causes for the different ENSO impacts on the North American temperature and precipitation, the 200-hPa geopotential height and 850-hPa wind vector composites using ERA20C are shown in Figs. 8 and 10 for the four SOM patterns (P1/P2 and P7/P8) and their differences. For the strong La Niña pattern 1 (Fig. 8a), the 200-hPa geopotential height shows
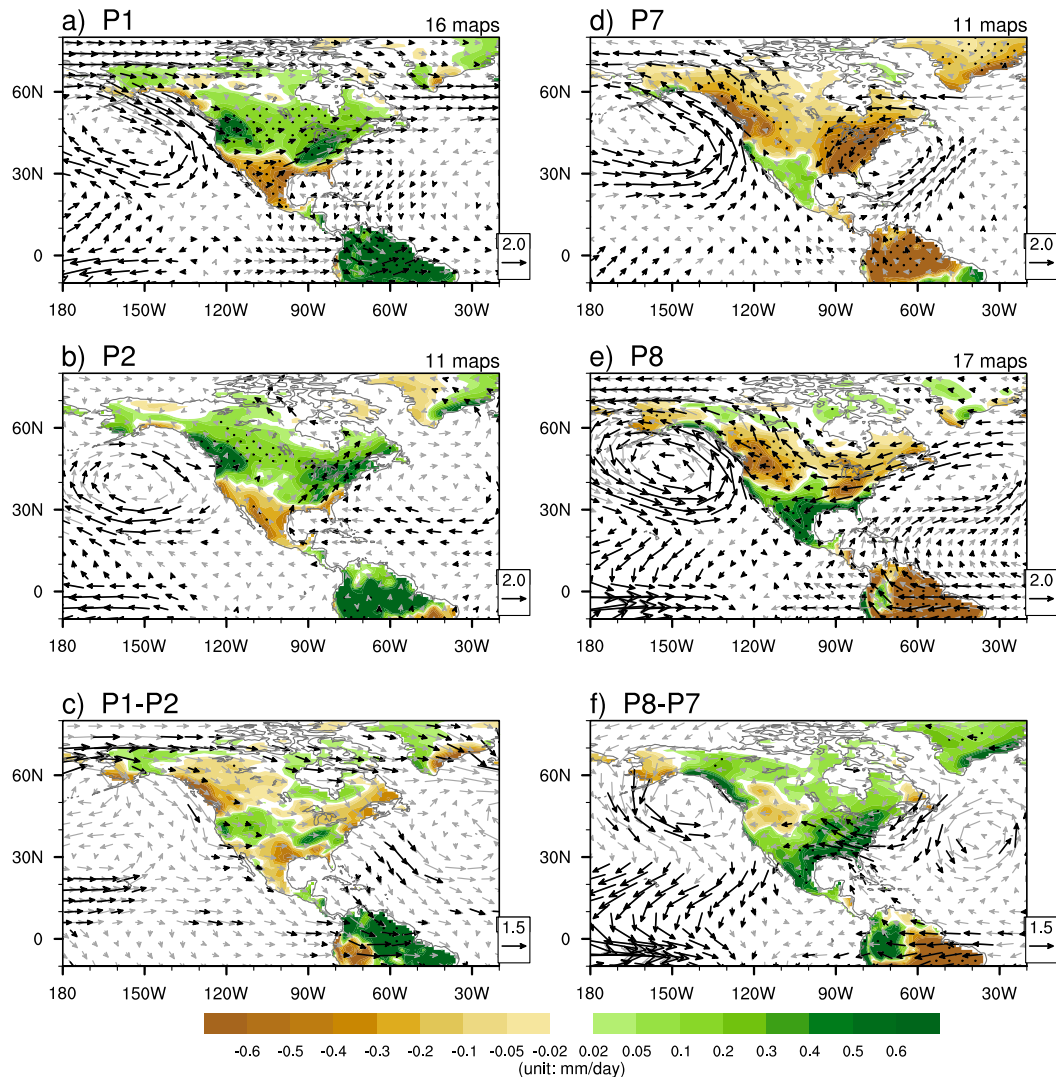
FIG. 10. Composite maps of the DJF-mean horizontal wind anomalies at 850 hPa over North America (vector; m s^{-1}) and land precipitation anomalies (shading; °C) based on (a),(b) the two La Niña patterns and (c) their differences and (d),(e) the two El Niño patterns and (f) their differences, with ERA20C for the period 1901–2010. The thick vectors and stippling indicate anomalies at or above the 90% confidence level using the two-tailed nonparametric Monte Carlo bootstrap statistical significance test.

that a pair of low pressure centers in the tropical eastern Pacific straddles the cold SST anomaly and east of the negative convection anomaly, very much consistent with a Matsuno–Gill type of solution (Matsuno 1966; Gill 1980). In the extratropics, the Rossby wave propagation leads to an anticyclone anomaly over the northern North Pacific, a cyclone anomaly in northwestern Canada, and a weak anticyclone anomaly over the southeastern United States at 200 hPa (Fig. 8a), following the great circle route illustrated in Hoskins and Karoly (1981). The combination of the anomalous tropical cyclone and the extratropical anticyclone in the subtropical Pacific results in a

reduced subtropical jet intensity and a northward-shifted storm track (e.g., Eichler and Higgins 2006), consistent with the dipole pattern of rainfall change with reduced rainfall in the south and increased rainfall to the north in Fig. 9a. The deeper trough over northwestern Canada coupled with the North Pacific anticyclone is conducive to the anomalous cold advection of frigid air from the Arctic (see significant wind vector anomalies there in Fig. 10a) and thus cold temperature anomalies there, whereas the anticyclone in the southeast United States and the lack of storminess favor a warmer-than-usual winter there. For pattern 2 with weak cooling in the equatorial central-eastern

Pacific, the geopotential height responses are less significant except the tropical features and the North Pacific anticyclone (Fig. 8b). The anticyclone anomaly response in the North Pacific between 30° and 55°N tends to be more zonal compared to that for P1 (significant differences there in Fig. 8c) and is linked to weak cooling in northwestern Canada. For the CP2 pattern 7 (Fig. 8d), there is a significant wave train pattern with a low in the Gulf of Alaska, a high over Canada and the western United States, and another low in the southeast United States, resembling the canonical Pacific–North American (PNA) pattern (Wallace and Gutzler 1981). The anomalous ridge in Canada extends from the western United States to Mexico, reduces the cold air advection from the north, and is associated with positive temperature anomalies there. The wave train in Fig. 8d resembles that in Fig. 8a for the strong La Niña pattern but with an opposite sign. The North American surface temperature patterns in both cases also share the southeast–northwest dipole with opposite sign, except that the CP2 pattern 7 tends to have a stronger east–west component in surface temperature anomalies owing to a stronger low pressure center in the southeast United States in Fig. 8d as compared to the corresponding feature in Fig. 8a. For the EP El Niño pattern 8 (Fig. 8e), there is a pair of strong tropical anticyclones straddling the warm SST anomaly, which is more than double the amplitude and about 10 degrees farther east of that in Fig. 8d for P7. The extratropical wave train response in Fig. 8e is similar to the tropical Northern Hemisphere (TNH) pattern identified by Mo and Livezey (1986). There is a strong enhancement of the subtropical westerlies at 30°N, which shifts the storm track farther south across the southern United States, leading to the wet south–dry north and cold south–warm north structure as seen in Figs. 9e and 7e, respectively. The major differences in North American temperature and precipitation responses to CP2 and EP, an east–west structure for CP2 and north–south structure for EP, seem to be related to the differences in Rossby wave propagation, with CP2 El Niño having a wave train originating from farther west compared to the EP. There are substantial differences between our composites for the two types of El Niño events and that shown in Yu et al. (2012), where they show a stronger and more zonally oriented geopotential height response to CP El Niño than that for EP El Niño. Despite differences in the identification of the two EL Niño types, Yu et al. (2012) also focused on late winter, January–March (JFM) rather than DJF. As shown in Jong et al. (2016), there are sensitivities in atmospheric response to El Niño SST as a function of season. Thus, it is difficult to parse out the exact cause of the discrepancies between our results and that of Yu

et al. (2012). The statistical significance of the results here based on both the height responses and the surface climate provide confidence to our method. Figure 8f further illustrates the statistically significant difference between P7 and P8, showing an anomalous low and cooler temperature over the west coast and a high anomaly and warmer temperature to Canada and the eastern United States for EP as compared to CP2 El Niño.

The low-level wind anomalies (Fig. 10) are consistent with the dominant features of the 200-hPa height pattern and indicate an equivalent barotropic structure in the extratropics. The two La Niña (El Niño) patterns are dominated by a significant anticyclone (cyclone) in the Gulf of Alaska and an anticyclone (cyclone) center off the U.S. southeast coast. While the north–south dipole in North American precipitation can largely be explained by the shift of jet and storm tracks northward (southward) associated with La Niña (El Niño) conditions (Figs. 10a,e), the detailed structures of the precipitation anomalies can be explained by the position and orientation of the low-level circulation features. For example, the robust drying in the eastern United States for CP2 pattern 7 (Fig. 10d) is associated with the northeasterly flow associated with the strong cyclonic flow over the eastern United States, which contrasts sharply with the more zonally oriented cyclonic flow that spans from the subtropical North Atlantic and the northern half of the United States for EP (Fig. 10e). The latter led to a more zonally oriented precipitation anomaly pattern that is dry north and wet south in the eastern half of the U.S., rather than drying throughout the eastern United States as in Fig. 10d. The differences between the two (Fig. 10f) are largely significant over the eastern United States in both the 850-hPa wind vectors and the precipitation. The contrast in 850-hPa wind anomalies between the two La Niña patterns is less significant (Fig. 10c).

Some sensitivity tests were performed to the composite SST, precipitation, surface temperature, and atmospheric circulation using subsets of the observational data, such as only using the post-1950 data to test the data reliability and removing some marginal events that have a relatively large Euclidean distance to the corresponding patterns. The results are generally insensitive to the different choices and are thus robust.

b. AGCM results

The observed composites as shown in Figs. 7–10 strongly suggest that differences in ENSO-related SST anomaly patterns may be responsible for the composite atmospheric responses to the different SOM SST patterns. Given the limited sample sizes for each SOM pattern (ranging from 11 to 17 winters), however, there may be
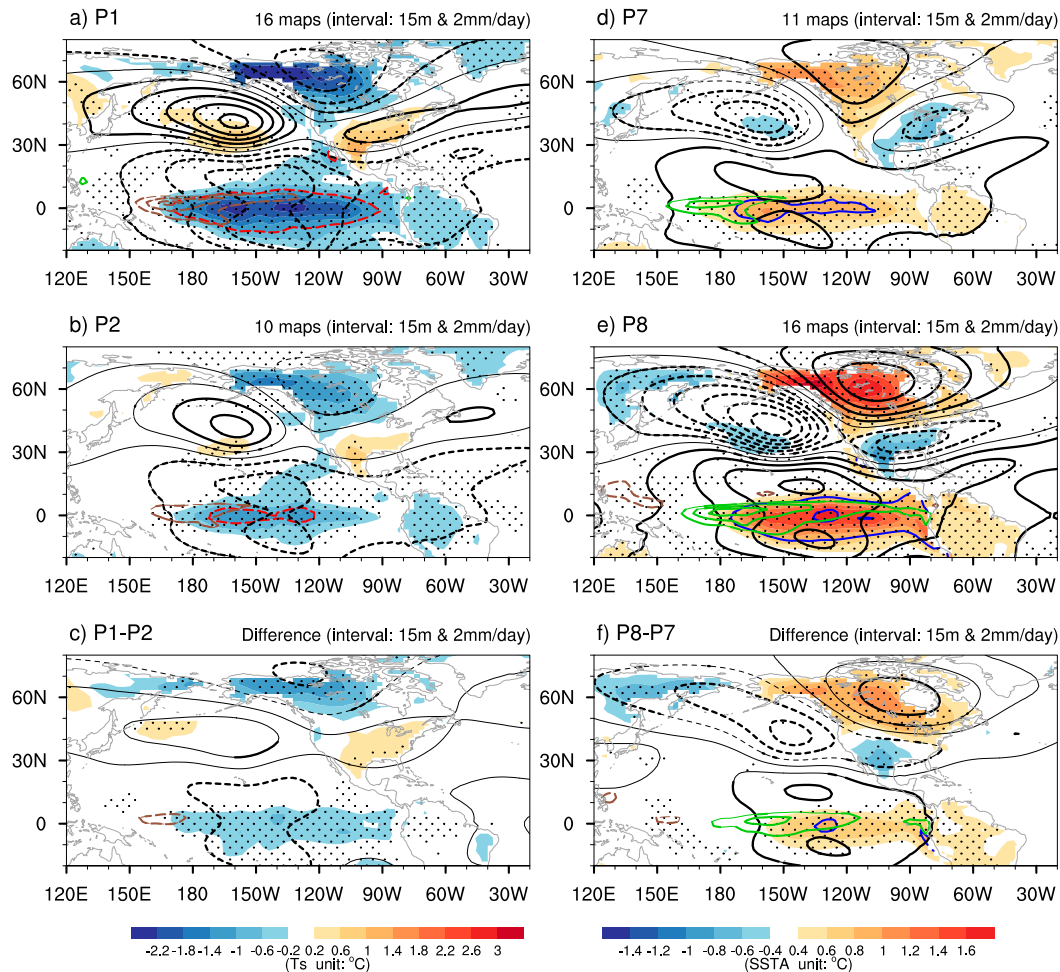
CAM4 Z_200 & Precip & Ts & SSTa. [1901-2008]

FIG. 11. As in Fig. 8, but for geopotential at 200 hPa, precipitation, and surface temperature from CAM4 16-member GOGA experiments.

internal atmospheric variability unrelated to the SST differences that could contribute to differences in the teleconnection patterns. The similar composites based on 16-member ensemble means of the AGCM experiment using NCAR CAM4 with prescribed observed global SST (CAM4 GOGA) are used in this subsection to better extract the SST-forced components. By averaging over 16 ensemble members with the same SST conditions, the internal variability is largely removed. Similar composite analysis as done for observations can then be used to determine whether the different teleconnections as seen in Figs. 7–10 are indeed forced by the SST differences.

The 200-hPa geopotential height and surface temperature composites for CAM4 are shown in Fig. 11, and the corresponding 850-hPa wind vectors and land precipitation anomalies are shown in Fig. 12. The 200-hPa height composites corresponding to the four SOM patterns are very well reproduced in CAM4, with a spatial

pattern correlation between each corresponding pattern exceeding 0.9 (Table 1). The westward-shifted and more meridionally propagating wave train for CP2 El Niño as compared to that for EP El Niño is well captured in CAM4 (Figs. 11d,e). As a result, the surface temperature differences between CP2 and EP are well reproduced in CAM4, with more of an east–west dipole in Fig. 11d as compared to the north–south dipole in Fig. 11e. However, the surface temperature difference between CP2 and EP is not as prominent in CAM4 compared to observations (Figs. 8f and 11f). The distinctive precipitation composites between P7 and P8 are somewhat simulated by CAM4, which shows a predominantly dry eastern United States for P7 (Fig. 12d) and a north dry–south wet pattern for P8 (Fig. 12e). The 850-hPa wind vectors between CAM4 composites and ERA20C reanalysis also suggest many similarities for all four patterns, with spatial pattern correlation coefficients

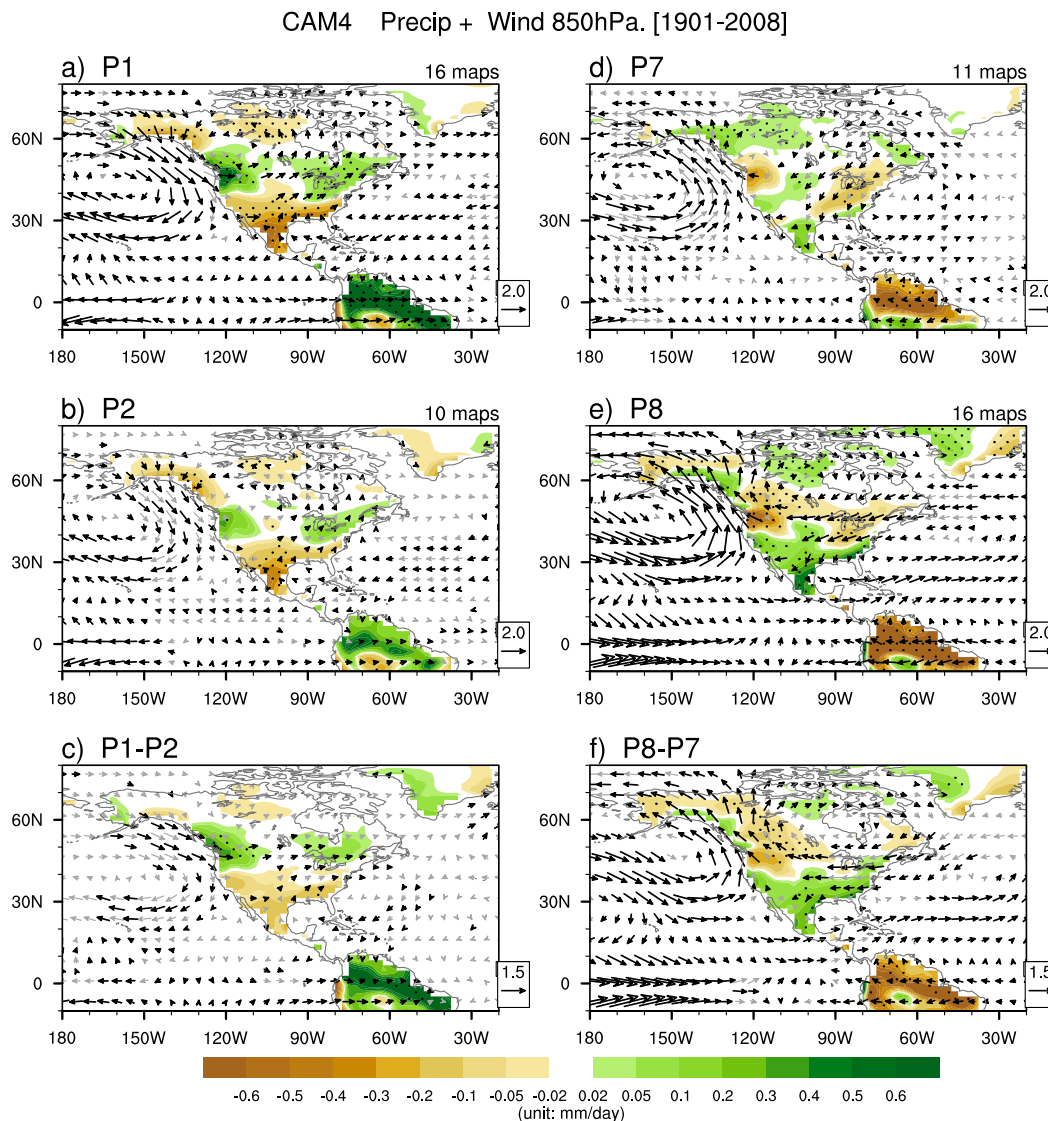## CAM4   Precip + Wind 850hPa. [1901-2008]

FIG. 12. As in Fig. 10, but for the horizontal wind at 850 hPa and land precipitation anomalies from CAM4
16-member GOGA experiments.

of 0.84 (0.76) and higher for the zonal (meridional) component. The similarity between CAM4 and the observational results indicates that the differences in teleconnection patterns and the North American climate are largely forced by the distinct SST anomaly patterns. Garfinkel et al. (2013) investigated the October–December (OND) and JFM mean surface temperature responses over North America to prescribed EP and CP El Niño SST anomalies using the Goddard Earth Observing System Chemistry–Climate Model. Their results of the different surface temperature responses to EP and CP El Niño are very similar to ours, which further confirms that these differences can be attributed to the SST anomaly patterns in the tropical Pacific.

We have also examined the similar GOGA experiments using CAM5, the newer version of the NCAR atmospheric model, and found that the differences between CP2 and EP were slightly less obvious compared to that in CAM4. While the CAM5 composites (not shown) capture some of the differences between CP2 and EP in its circulation patterns, the anticyclone anomaly over Canada does not extend as far south along the west coast as in CAM4 and observations for CP2, thus favoring a north–south dipole for surface temperature over North America for P7. The area-weighted spatial pattern correlation between CAM4 (CAM5) and ERA20C 200-hPa geopotential height and 850-hPa zonal and meridional wind composites (Table 1)

TABLE 1. The area-weighted spatial pattern correlation coefficients of 200-hPa geopotential height and 850-hPa horizontal wind composites between ERA20C and CAM4 (CAM5) for the domain shown in Figs. 7 and 8.

		P1	P2	P7	P8	P1 − P2	P8 − P7
200 hPa *Z*	CAM4	0.96	0.90	0.92	0.95	0.76	0.72
	CAM5	0.96	0.90	0.93	0.96	0.84	0.76
850 hPa *U*(*V*)	CAM4	0.90(0.85)	0.84(0.76)	0.85(0.77)	0.92(0.86)	0.21(0.42)	0.52(0.64)
	CAM5	0.91(0.85)	0.85(0.70)	0.85(0.72)	0.91(0.90)	0.40(0.56)	0.71(0.60)

indicates that while both models correlate well with observations, the 850-hPa meridional wind for P2 and P7 shows a higher correlation for CAM4 than CAM5 and for P8, the opposite is true. Overall, the meridional wind component is less well simulated by CAM4 and CAM5 compared to the other variables, and P2 and P7 composites in AGCMs are less similar to observations. The lack of distinction in CAM5 simulations of the surface temperature and precipitation responses to different patterns of SST is possibly related to the inability of the model to simulate a more meridional structure of the wave train in P7. Upon further examination, the difference between CAM4 and CAM5's response to CP2 SST pattern is mainly due to the location and strength of the tropical convection centers. We found that the tropical convection response to CP2 SST pattern in CAM4 is stronger and shifts farther westward than that in CAM5, resulting in more meridional wave propagation in CAM4. It is interesting to note that while AGCMs such as CAM5 are well known to be able to simulate the canonical ENSO responses well, the accuracy of these models in simulating the inter–El Niño differences is not well established. The latter model skill is essential for accurate seasonal climate prediction of regional climate anomalies based on ENSO SST.

c. *Role of internal atmospheric variability*

All the observational results obtained in the present work contained both the effect of internal variability of climate system and the SST-forced component. The CAM4 ensemble mean largely mutes the internal variability and highlights the SST-forced signal, which could be considered as an indication that the composite teleconnection responses were mainly forced by the SST anomaly pattern. However, some studies have noted the important role of internal atmospheric variability in influencing the atmospheric response to ENSO events (Kumar and Hoerling 1997). It is worthwhile to examine further how internal variability may impact the atmospheric responses to the different patterns of SST anomaly as identified here.

The composite analyses were performed using each individual CAM4 ensemble member (16 total) for P1/P2

and P7/P8. These model composites are then compared to the corresponding observed composite using spatial pattern correlations for surface temperature over North America (0°–65°N, 210°–310°E) and 200-hPa geopotential height for the domain as shown in Fig. 8 (20°S–80°N, 120°–340°E). The cross-pattern correlations between P1 and P2 and between P7 and P8 are also computed. The correlation coefficients are summarized in Fig. 13 in the box diagram. One notices that the ensemble spread in spatial pattern correlations is the largest for P2, which is the weak La Niña pattern. In fact the cross correlation between model P2 and observed P1 is higher than that with observed P2. This indicates that some model ensembles show a stronger response to the weak La Niña as compared to the corresponding observations. Given that the observed composite for P2 is mostly not statistically significant outside of the tropics, it is perhaps not surprising that the internal variability would be contributing more to the atmospheric response to SST anomalies than in the stronger SST forcing case, such as P1 and P8. The model spread is also rather large for P7, but mainly owing to one outlier among the 16 members, and the same pattern correlation is consistently higher than the cross-pattern correlation in the case of P7. For the two strong cases (P1 and P8), the ensemble spread is rather small and the same-pattern correlation is generally larger than the cross-pattern correlation, indicating that the composites are largely dominated by the SST-forced component.

We conclude that while internal variability definitely can contribute to uncertainties in atmospheric response to a given SST forcing, the SOM-identified SST patterns, with the exception of the weak La Niña, all show a robust response that is consistent with the observational composite, and the two El Niño patterns are distinguishable in most of the GCM ensemble members. Thus, the observed differences, as seen in Figs. 8 and 9, can be taken as mostly due to their SST pattern differences (including both amplitude and spatial patterns).

5. Summary and discussion

Eight different SST anomaly patterns in the tropical Pacific were identified by the SOM analysis in this study.
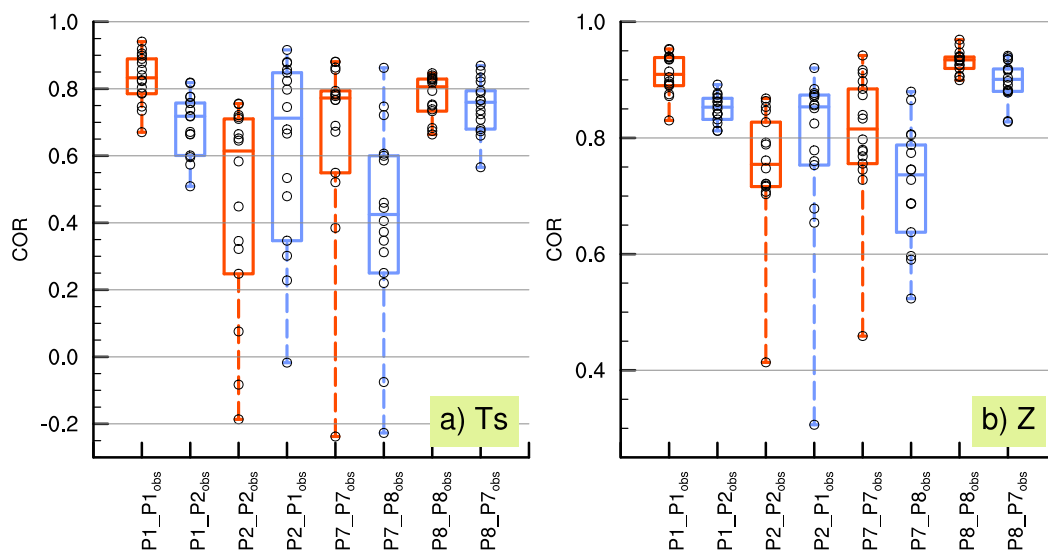
FIG. 13. Box plot of the spatial correlation coefficients of (left) surface temperature and (right) 200-hPa geopotential height composites with hollow circles, indicating the spatial correlation between the observation and each ensemble member for each of the four patterns (P1 and P2, P7 and P8). The red (blue) box represents the correlation coefficients between the same (cross) patterns.

Two of the eight (P4 and P5) represent near-normal states in the tropical Pacific with little SST anomalies, and the other six SOM patterns show distinct features in the amplitude and, in some cases, longitudinal locations of SST anomaly. The SST anomaly patterns 1–3 exhibit three strong to weak La Niña–like SST patterns in the equatorial central-eastern Pacific. The last three patterns 6–8 reveal one weak CP El Niño–like pattern, one with warming both in the CP and EP (termed CP2), and one EP El Niño–like pattern. The corresponding tropical convection shows distinct differences in both the intensity and the location of the anomalous convection. Hence, the tropically forced wave train also differs leading to sensitivities in teleconnection patterns.

The impact of each SOM pattern on North American climate during boreal winter shows distinct differences between the two significant La Niña (P1 and P2) and two El Niño patterns (P7 and P8). For the strong La Niña (P1) and EP El Niño (P8), the precipitation and surface temperature show a north–south dipole over North America, with wet/cold (dry/warm) north and dry/warm (wet/cold) south for La Niña (El Niño). These distinct differences are well known and can be attributed to the differing barotropic wave train patterns induced by differing tropical convection patterns, which can lead to the reduced (enhanced) subtropical jet intensity and a northward (southward)-shifted storm track. For La Niña pattern 2, a more zonal but less significant teleconnection structure compared to that for P1 is observed, linking to weak warming over the southern United

States and cooling over northwestern Canada. The CP2 El Niño (P7) features a distinctive east–west dipole pattern of surface temperature anomaly over the United States, which is linked to a more meridionally oriented Rossby wave train originated from the central tropical Pacific, similar to the PNA pattern. Additionally, there are significant drying anomalies in the eastern United States for CP2 El Niño winters (P7), associated with the northeasterly flow there. The results of CAM4 GOGA experiments confirm the observed atmospheric teleconnection responses to the different SOM patterns, further suggesting that the significant differences of North American surface temperature and precipitation changes are indeed due to the distinct SST anomaly patterns. However, it is noted that the differences in the atmospheric circulation responses to different SST patterns in CAM5 were less obvious than that in CAM4, though CAM5 captures better the response to canonical EP El Niño. The discrepancies between the two models are perhaps caused by how sensitive these models' tropical convection responds to the central versus eastern Pacific SST anomalies.

However, it should be noted that large differences in SST anomaly amplitude among different SOM patterns exist between P1 and P2 and between P7 and P8. To further explore the sensitivity of the teleconnection to the SST anomaly amplitude, we divided the El Niño and La Niña events into four groups according to the DJF-mean Niño-3.4 index values (strong La Niña: Niño-3.4 ≤ -1.0; weak La Niña: $-1.0 <$ Niño-3.4 ≤ -0.5; weak El Niño:
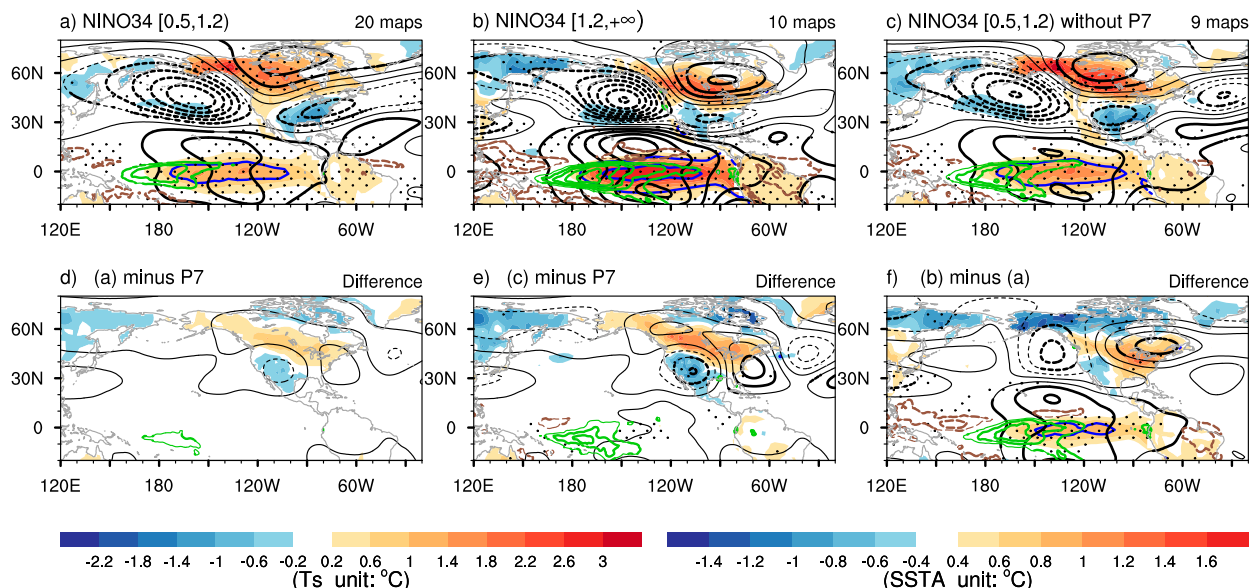
FIG. 14. (a)–(c) Composite of the sea surface temperature anomalies (shading over ocean and blue contour; °C), surface temperature (shading over land; °C), 200-hPa geopotential height in m (black contour), precipitation (green and brown contour; mm day^{-1}) according to the (left),(center) Niño-3.4-based El Niño cases and (right) some without the overlapping events for the warm phase. Difference between (d) the weak El Niño events and P7 (shown as Fig. 8d), (e) non-P7 weak El Niño events and P7, and (f) the strong and weak El Niño cases. The contour interval for precipitation is 2 mm day^{-1}. The contour interval for SST anomaly is 0.8°C, starting from 0.8°C. The thick contours and stippling indicate values at or above the 90% confidence level using the two-tailed nonparametric Monte Carlo bootstrap statistical significance test.

0.5 ≤ Niño-3.4 < 1.2; and strong El Niño: Niño-3.4 ≥ 1.2). For the cold phase, we identified 13 strong and 18 weak La Niña events. The composite patterns of teleconnection and North American climate anomaly for the strong and weak La Niña cases are similar to that for P1 and P2, respectively, and their differences are not significant (figures not shown). This indicates that the La Niña patterns identified by SOM are largely distinguished by their SST anomaly amplitude. For the warm phase, we identified 20 weak El Niño cases and 10 strong El Niño events. Their composite patterns are shown in Figs. 14a,b. All 10 strong El Niño events were identified as P8 events, while 11 of the 20 weak El Niño events were identified as P7. Given the large overlap, we further divided the weak events to those not part of P7, shown in Fig. 14c. A visual inspection shows some difference between weak El Niño and P7 composites (Fig. 14a vs Fig. 8d), but the difference map shows no statistical significance (Fig. 14d). Given the large overlap between weak events and P7 events, this is perhaps not surprising. When we subtract the weak events without the overlapping events, however, the differences (Fig. 14e) are significant, with a dipole pattern with a low over the western United States and a high over the east coast of United States. We further ask if the difference purely due to El Niño amplitude is similar to or different from the difference between P7 and P8 patterns (as shown in

Fig. 8f), which has both the amplitude and the spatial pattern differences. Figure 14f exhibits the difference map between strong and weak El Niño composites, showing a dipole that is shifted to the west compared to the one that is due to the two pattern differences (Fig. 8f), and the associated temperature differences are much stronger for P8 minus P7 than strong minus weak El Niño. This suggests that the spatial pattern difference in SST must have contributed to a more significant wave train pattern over North America and the associated temperature anomalies in Fig. 8f.

We note that it is difficult to unambiguously separate the amplitude versus spatial structure contributions to P7 and P8 differences given limited sample. However Fig. 14 provides some evidence that there is more than simply the weak versus strong El Niño that separates the two El Niño patterns identified by the SOM method. Thus, the SOM identification may supply some useful information to better understand the characterization of different ENSO events and their impact on the extratropical climate. However, we recognize the limitations of the cluster method given the multitudes of different ENSO flavors.

Each ENSO event is unique in both its SST anomaly patterns and the climate responses. The results in this study suggest that for accurate ENSO-based seasonal climate prediction, it is essential for coupled climate

models to simulate both the amplitude and spatial structure of the SST anomalies. Furthermore, it requires the model to have high skill in correctly representing the sensitivity of the teleconnection to the detailed structures of the SST anomalies. The lack of model skills in forecasting such a response provides an interesting case for further understanding. Further diagnosis for the different sensitivity in CAM4 and CAM5 models and other AGCMs may shed light on the most relevant processes needed for simulating the distinct climate responses to the different ENSO flavors.

REFERENCES

Ashok, K., S. K. Behera, S. A. Rao, H. Weng, and T. Yamagata, 2007: El Niño Modoki and its possible teleconnection. *J. Geophys. Res.*, **112**, C11007, doi:10.1029/2006JC003798.

Benjamini, Y., and Y. Hochberg, 1995: Controlling the false discovery rate: A practical and powerful approach to multiple testing. *J. Roy. Stat. Soc.*, **57B**, 289–300.

Cai, W., and T. Cowan, 2009: La Niña Modoki impacts Australia autumn rainfall variability. *Geophys. Res. Lett.*, **36**, L12805, doi:10.1029/2009GL037885.

Capotondi, A., and Coauthors, 2015: Understanding ENSO diversity. *Bull. Amer. Meteor. Soc.*, **96**, 921–938, doi:10.1175/BAMS-D-13-00117.1.

Chen, Z., Z. Wen, R. Wu, P. Zhao, and J. Cao, 2014: Influence of two types of El Niños on the East Asian climate during boreal summer: A numerical study. *Climate Dyn.*, **43**, 469–481, doi:10.1007/s00382-013-1943-1.

Chiodi, A. M., and D. E. Harrison, 2013: Impacts on seasonal U.S. atmospheric circulation, temperature, and precipitation anomalies: The OLR-event perspective. *J. Climate*, **26**, 822–837, doi:10.1175/JCLI-D-12-00097.1.

——, and ——, 2015: Global seasonal precipitation anomalies robustly associated with El Niño and La Niña Events—An OLR perspective. *J. Climate*, **28**, 6133–6159, doi:10.1175/JCLI-D-14-00387.1.

Choi, J., S.-I. An, J.-S. Kug, and S.-W. Yeh, 2011: The role of mean state on changes in El Niño flavor. *Climate Dyn.*, **37**, 1205–1215, doi:10.1007/s00382-010-0912-1.

Christiansen, B., 2007: Atmospheric circulation regimes: Can cluster analysis provide the number? *J. Climate*, **20**, 2229–2250, doi:10.1175/JCLI4107.1.

Compo, G. P., and Coauthors, 2011: The Twentieth Century Reanalysis Project. *Quart. J. Roy. Meteor. Soc.*, **137**, 1–28, doi:10.1002/qj.776.

Eichler, T., and W. Higgins, 2006: Climatology and ENSO-related variability of North American extratropical cyclone activity. *J. Climate*, **19**, 2076–2093, doi:10.1175/JCLI3725.1.

Garfinkel, C. I., M. Hurwitz, D. Waugh, and A. Butler, 2013: Are the teleconnections of central Pacific and eastern Pacific El Niño distinct in boreal wintertime? *Climate Dyn.*, **41**, 1835–1852, doi:10.1007/s00382-012-1570-2.

Gill, A. E., 1980: Some simple solutions for heat-induced tropical circulation. *Quart. J. Roy. Meteor. Soc.*, **106**, 447–462, doi:10.1002/qj.49710644905.

Graham, F. S., J. N. Brown, C. Langlais, S. J. Marsland, A. T. Wittenberg, and N. J. Holbrook, 2014: Effectiveness of the Bjerknes stability index in representing ocean dynamics. *Climate Dyn.*, **43**, 2399–2414, doi:10.1007/s00382-014-2062-3.

Harris, I., P. D. Jones, T. J. Osborn, and D. H. Lister, 2014: Updated high-resolution grids of monthly climatic observations—The CRU TS3.10 dataset. *Int. J. Climatol.*, **34**, 623–642, doi:10.1002/joc.3711.

Harrison, D. E., and N. K. Larkin, 1998: El Niño–Southern Oscillation sea surface temperature and wind anomalies, 1946–1993. *Rev. Geophys.*, **36**, 353–400, doi:10.1029/98RG00715.

Hastie, T., R. Tibshirani, and J. Friedman, 2009: Unsupervised learning. *The Elements of Statistical Learning: Data Mining, Inference, and Prediction*, 2nd ed. T. Hastie, R. Tibshirani, and J. Friedman, Eds., Springer, 485–585.

Hewitson, B. C., and R. G. Crane, 2002: Self-organizing maps: Applications to synoptic climatology. *Climate Res.*, **22**, 13–26, doi:10.3354/cr022013.

Hoerling, M. P., A. Kumar, and M. Zhong, 1997: El Niño, La Niña, and the nonlinearity of their teleconnections. *J. Climate*, **10**, 1769–1786, doi:10.1175/1520-0442(1997)010<1769:ENOLNA>2.0.CO;2.

Horel, J. D., and J. M. Wallace, 1981: Planetary-scale atmospheric phenomena associated with the Southern Oscillation. *Mon. Wea. Rev.*, **109**, 813–829, doi:10.1175/1520-0493(1981)109<0813:PSAPAW>2.0.CO;2.

Hoskins, B. J., and D. J. Karoly, 1981: The steady linear response of a spherical atmosphere to thermal and orographic forcing. *J. Atmos. Sci.*, **38**, 1179–1196, doi:10.1175/1520-0469(1981)038<1179:TSLROA>2.0.CO;2.

Infanti, J. M., and B. P. Kirtman, 2016: North American rainfall and temperature prediction response to the diversity of ENSO. *Climate Dyn.*, **46**, 3007–3023, doi:10.1007/s00382-015-2749-0.

Iskandar, I., 2009: Variability of satellite-observed sea surface height in the tropical Indian Ocean: Comparison of EOF and SOM analysis. *Makara J. Sci.*, **13**, 173–179, doi:10.7454/mss.v13i2.421.

Johnson, N. C., 2013: How many ENSO flavors can we distinguish?. *J. Climate*, **26**, 4816–4827, doi:10.1175/JCLI-D-12-00649.1.

——, and Y. Kosaka, 2016: The impact of eastern equatorial Pacific convection on the diversity of boreal winter El Niño teleconnection patterns. *Climate Dyn.*, **47**, 3737–3765, doi:10.1007/s00382-016-3039-1.

——, S. B. Feldstein, and B. Tremblay, 2008: The continuum of Northern Hemisphere teleconnection patterns and a description of the NAO shift with the use of self-organizing maps. *J. Climate*, **21**, 6354–6371, doi:10.1175/2008JCLI2380.1.

Jong, B.-T., M. Ting, and R. Seager, 2016: El Niño's impact on California precipitation: Seasonality, regionality, and El Niño intensity. *Environ. Res. Lett.*, **11**, 054021, doi:10.1088/1748-9326/11/5/054021.

Kao, H.-Y., and J.-Y. Yu, 2009: Contrasting eastern-Pacific and central-Pacific types of ENSO. *J. Climate*, **22**, 615–632, doi:10.1175/2008JCLI2309.1.

Kohonen, T., 1998: The self-organizing map. *Neurocomputing*, **21**, 1–6, doi:10.1016/S0925-2312(98)00030-7.

——, 2001: *Self-Organizing Maps*. 3rd ed. Springer, 501 pp.

——, J. Hynninen, J. Kangas, and J. Laaksonen, 1995: SOM_PAK: The self-organizing maps program package. Helsinki University of Technology Rep., 27 pp. [Available online at http://www.cis.hut.fi/research/som_pak/som_doc.txt.]

Kug, J.-S., and Y. G. Ham, 2011: Are there two types of La Niña? *Geophys. Res. Lett.*, **38**, L16704, doi:10.1029/2011GL048237.

——, F. Jin, and S.-I. An, 2009: Two types of El Niño events: Cold tongue El Niño and warm pool El Niño. *J. Climate*, **22**, 1499–1515, doi:10.1175/2008JCLI2624.1.

Kumar, A., and M. P. Hoerling, 1997: Interpretation and implications of the observed inter–El Niño variability. *J. Climate*, **10**, 83–91, doi:10.1175/1520-0442(1997)010<0083:IAIOTO>2.0.CO;2.

Larkin, N. K., and D. E. Harrison, 2005a: On the definition of El Niño and associated seasonal average U.S. weather anomalies. *Geophys. Res. Lett.*, **32**, L13705, doi:10.1029/2005GL022738.

——, and ——, 2005b: Global seasonal temperature and precipitation anomalies during El Niño autumn and winter. *Geophys. Res. Lett.*, **32**, L16705, doi:10.1029/2005GL022860.

Lau, N. C., A. Leetmaa, and M. J. Nath, 2008: Interactions between the responses of North American climate to El Niño–La Niña and to the secular warming trend in the Indian–western Pacific Oceans. *J. Climate*, **21**, 476–494, doi:10.1175/2007JCLI1899.1.

Leloup, J., Z. Lachkar, J.-P. Boulanger, and S. Thiria, 2007: Detecting decadal changes in ENSO using neural networks. *Climate Dyn.*, **28**, 147–162, doi:10.1007/s00382-006-0173-1.

L'Heureux, M. L., D. C. Collins, and Z.-Z. Hu, 2013: Linear trends in sea surface temperature of the tropical Pacific Ocean and implications for the El Niño–Southern Oscillation. *Climate Dyn.*, **40**, 1223–1236, doi:10.1007/s00382-012-1331-2.

——, M. K. Tippett, and A. G. Barnston, 2015: Characterizing ENSO coupled variability and its impact on North American seasonal precipitation and temperature. *J. Climate*, **28**, 4231–4245, doi:10.1175/JCLI-D-14-00508.1.

Li, X., C. Li, J. Ling, and Y. Tan, 2015: The relationship between contiguous El Niño and La Niña revealed by self-organizing maps. *J. Climate*, **28**, 8118–8134, doi:10.1175/JCLI-D-15-0123.1.

Liebmann, B., and C. A. Smith, 1996: Description of a complete (interpolated) outgoing longwave radiation dataset. *Bull. Amer. Meteor. Soc.*, **77**, 1275–1277.

Lin, G.-F., and L.-H. Chen, 2006: Identification of homogeneous regions for regional frequency analysis using the self-organizing map. *J. Hydrol.*, **324**, 1–9, doi:10.1016/j.jhydrol.2005.09.009.

Liu, Y., R. H. Weisberg, and C. N. K. Mooers, 2006: Performance evaluation of the self-organizing map for feature extraction. *J. Geophys. Res.*, **111**, C05018, doi:10.1029/2006JA011890.

Matsuno, T., 1966: Quasi-geostrophic motions in the equatorial area. *J. Meteor. Soc. Japan*, **44**, 25–43.

Michelangeli, P.-A., R. Vautard, and B. Legras, 1995: Weather regimes: Recurrence and quasi stationarity. *J. Atmos. Sci.*, **52**, 1237–1256, doi:10.1175/1520-0469(1995)052<1237:WRRAQS>2.0.CO;2.

Mo, K. C., 2010: Interdecadal modulation of the impact of ENSO on precipitation and temperature over the United States. *J. Climate*, **23**, 3639–3656, doi:10.1175/2010JCLI3553.1.

——, and R. E. Livezey, 1986: Tropical-extratropical geopotential height teleconnections during the Northern Hemisphere winter. *Mon. Wea. Rev.*, **114**, 2488–2515, doi:10.1175/1520-0493(1986)114<2488:TEGHTD>2.0.CO;2.

Neale, R. B., and Coauthors, 2010: Description of the NCAR Community Atmosphere Model (CAM 4.0). NCAR Tech. Note NCAR/TN-485+STR, 224 pp. [Available online at http://www.cesm.ucar.edu/models/ccsm4.0/cam/docs/description/cam4_desc.pdf.]

——, and Coauthors, 2012: Description of the NCAR Community Atmosphere Model (CAM 5.0). NCAR Tech. Note NCAR/TN-486+STR, 289 pp. [Available online at http://www.cesm.ucar.edu/models/cesm1.0/cam/docs/description/cam5_desc.pdf.]

Poli, P., and Coauthors, 2013: The data assimilation system and initial performance evaluation of the ECMWF pilot reanalysis of the 20th-century assimilating surface observations only (ERA-20C). ERA Rep. Series 14, 62 pp. [Available online at http://www.ecmwf.int/sites/default/files/elibrary/2013/11699-data-assimilation-system-and-initial-performance-evaluation-ecmwf-pilot-reanalysis-20th.pdf.]

Rasmusson, E. M., and T. H. Carpenter, 1982: Variation in tropical sea surface temperature and surface wind fields associated with the Southern Oscillation/El Niño. *Mon. Wea. Rev.*, **110**, 354–384, doi:10.1175/1520-0493(1982)110<0354:VITSST>2.0.CO;2.

Rayner, N. A., D. E. Parker, E. B. Horton, C. K. Folland, L. V. Alexander, D. P. Powell, E. C. Kent, and A. Kaplan, 2003: Global analysis of sea surface temperature, sea ice, and night marine air temperature since the late nineteenth century. *J. Geophys. Res.*, **108**, 4407, doi:10.1029/2002JD002670.

Ren, H. L., and F. F. Jin, 2011: Niño indices for two types of ENSO. *Geophys. Res. Lett.*, **38**, L04704, doi:10.1029/2010GL046031.

Reusch, D. B., R. B. Alley, and B. C. Hewitson, 2005: Relative performance of self-organizing maps and principal component analysis in pattern extraction from synthetic climatological data. *Polar Geogr.*, **29**, 188–212, doi:10.1080/789610199.

Richardson, A. J., C. Risien, and F. A. Shillington, 2003: Using self-organizing maps to identify patterns in satellite imagery. *Prog. Oceanogr.*, **59**, 223–239, doi:10.1016/j.pocean.2003.07.006.

Riddle, E. E., M. B. Stoner, N. C. Johnson, M. L. L'Heureux, D. C. Collins, and S. B. Feldstein, 2013: The impact of the MJO on clusters of wintertime circulation anomalies over the North American region. *Climate Dyn.*, **40**, 1749–1766, doi:10.1007/s00382-012-1493-y.

Ropelewski, C. F., and M. S. Halpert, 1986: North America precipitation and temperature associated with the El Niño/Southern Oscillation (ENSO). *Mon. Wea. Rev.*, **114**, 2352–2362, doi:10.1175/1520-0493(1986)114<2352:NAPATP>2.0.CO;2.

Rudolf, B., A. Becker, U. Schneider, A. Meyer-Christoffer, and M. Ziese, 2010: The new "GPCC full data reanalysis version 5" providing high-quality gridded monthly precipitation data for the global land-surface is public available since December 2010. GPCC Status Rep., 7 pp. [Available online at https://www.dwd.de/DE/leistungen/wzn/publikationen/GPCC_status_report_2010.pdf?__blob=publicationFile&v=2.]

Shinoda, T., H. E. Hurlburt, and E. J. Metzger, 2011: Anomalous tropical ocean circulation associated with La Niña Modoki. *J. Geophys. Res.*, **116**, C12001, doi:10.1029/2011JC007304.

Simmons, A. J., 1982: The forcing of stationary wave motion by tropical diabatic heating. *Quart. J. Roy. Meteor. Soc.*, **108**, 503–534, doi:10.1002/qj.49710845703.

Singh, A., 2012: Contrasting the flavors of ENSO and related trends in the tropical Pacific Ocean in recent decades. Thèse doctorat, Université Paul Sabatier Toulouse III, 181 pp. [Available online at https://tel.archives-ouvertes.fr/tel-00795552/file/Singh_these.pdf.]

Takahashi, K., A. Montecinos, K. Goubanova, and B. Dewitte, 2011: ENSO regimes: Reinterpreting the canonical and Modoki El Niño. *Geophys. Res. Lett.*, **38**, L10704, doi:10.1029/2011GL047364.

Trenberth, K. E., 1997: The definition of El Niño. *Bull. Amer. Meteor. Soc.*, **78**, 2771–2777, doi:10.1175/1520-0477(1997)078<2771: TDOENO>2.0.CO;2.

Vesanto, J., J. Himberg, E. Alhoniemi, and J. Parhankangas, 2000: SOM toolbox for Matlab 5. Helsinki University of Technology. [Available online at http://www.cis.hut.fi/projects/somtoolbox/.]

Wallace, J. M., and D. S. Gutzler, 1981: Teleconnections in the geopotential height field during the Northern Hemisphere winter. *Mon. Wea. Rev.*, **109**, 784–812, doi:10.1175/ 1520-0493(1981)109<0784:TITGHF>2.0.CO;2.

Wilks, D. S., 2006: On "field significance" and the false discovery rate. *J. Appl. Meteor. Climatol.*, **45**, 1181–1189, doi:10.1175/JAM2404.1.

Xu, G., T. J. Osborn, A. J. Matthews, and M. M. Joshi, 2015: Different atmospheric moisture divergence responses to extreme and moderate El Niño. *Climate Dyn.*, **47**, 393–410, doi:10.1007/ s00382-015-2844-2.

Yeh, S.-W., J.-S. Kug, B. Dewitte, M.-H. Kwon, B. Kirtman, and F.-F. Jin, 2009: El Niño in a changing climate. *Nature*, **461**, 511–514, doi:10.1038/nature08316.

Yu, B., X. Zhang, H. Lin, and J.-Y. Yu, 2015: Comparison of wintertime North American climate impacts associated with

multiple ENSO indices. *Atmos.–Ocean*, **53**, 426–445, doi:10.1080/07055900.2015.1079697.

Yu, J.-Y., and S. T. Kim, 2010: Identification of central-Pacific and eastern-Pacific types of ENSO in CMIP3 models. *Geophys. Res. Lett.*, **37**, L15705, doi:10.1029/2010GL044082.

——, and Y. Zou, 2013: The enhanced drying effect of central-Pacific El Niño on US winter. *Environ. Res. Lett.*, **8**, 014019, doi:10.1088/1748-9326/8/1/014019.

——, ——, S. T. Kim, and T. Lee, 2012: The changing impact of El Niño on US winter temperatures. *Geophys. Res. Lett.*, **39**, L15702, doi:10.1029/2012GL052483.

Yuan, Y., and H. M. Yan, 2013: Different types of La Niña events and different responses of the tropical atmosphere. *Chin. Sci. Bull.*, **58**, 406–415, doi:10.1007/s11434-012-5423-5.

Zhang, T., M. P. Hoerling, J. Perlwitz, D.-Z. Sun, and D. Murray, 2011: Physics of U.S. surface temperature response to ENSO. *J. Climate*, **24**, 4874–4887, doi:10.1175/2011JCLI3944.1.

Zhang, W., L. Wang, B. Xiang, L. Qi, and J. He, 2015: Impact of two types of La Niña on the NAO during boreal winter. *Climate Dyn.*, **44**, 1351–1366, doi:10.1007/s00382-014-2155-z.

Zou, Y., J.-Y. Yu, T. Lee, M.-M. Lu, and S. T. Kim, 2014: CMIP5 model simulations of the impacts of the two types of El Niño on the U.S. winter temperature. *J. Geophys. Res. Atmos.*, **119**, 3076–3092, doi:10.1002/2013JD021064.